Modeling of Laser Guide Star Wavefront Sensing for Extremely Large Telescopes

by

Kate Jackson
B.Sc., University of British Columbia, 2008

A Thesis Submitted in Partial Fulfillment of the
Requirements for the Degree of

Master of Applied Science

in the Department of Mechanical Engineering

Modeling of Laser Guide Star Wavefront Sensing for Extremely Large Telescopes

by

Kate Jackson
B.Sc., University of British Columbia, 2008

Supervisory Committee

Dr. Colin Bradley, Supervisor
(Department of Mechanical Engineering)

Dr. Nick Dechev, Departmental Member
(Department of Mechanical Engineering)

Dr. Pan Agathoklis, Outside Member
(Department of Electrical and Computer Engineering)

Supervisory Committee

Dr. Colin Bradley, Supervisor
(Department of Mechanical Engineering)

Dr. Nick Dechev, Departmental Member
(Department of Mechanical Engineering)

Dr. Pan Agathoklis, Outside Member
(Department of Electrical and Computer Engineering)

ABSTRACT

This thesis presents a simulation of the control system for Laser Guide Star (LGS) wavefront sensing of the Narrow Field Infrared Adaptive Optics System (NFIRAOS) which will be the Adaptive Optics (AO) system on the Thirty Meter Telescope. The control system is multirate and combines data from multiple sources, both natural and artificial, to provide wavefront correction. Artificial guide stars are generated by exciting atoms in the mesospheric sodium (Na) layer.

The characteristics of the Na layer have been examined; its variability, altitude and thickness will lead to false atmospheric turbulence measurements by AO systems integrated with Extremely Large Telescopes. A periodically updated constrained matched filter algorithm has been implemented in the control system simulation in order to gauge its ability to mitigate these effects.

The control system has also been implemented on the University of Victoria LGS Test Bench which reproduces wavefront measurements as they will be made by several of the wavefront sensors of NFIRAOS. The simulation has provided insight into the stability of the proposed control system and allowed necessary improvements to be made. It has been shown to meet the requirements of stability over long term with fast convergence. The matched filter algorithm has been shown to effectively reject the Na layer fluctuations both in simulation and on the test bench.

Contents

List of Figures

List of Tables

List of Acronyms

AO	Adaptive Optics
ACURA	Association of Canadian Universities for Research in Astronomy
CCD	Charge–Coupled Device
CoG	Centre of Gravity
DAQ	Digital Acquisition
DLL	Delay–Locked Loop
DM	Deformable Mirror
E-ELT	European Extremely Large Telescope
ELT	Extremely Large Telescope
ESO	European Southern Observatory
FSM	Fast Steering Mirror
FWHM	full width at half the maximum
GMT	Giant Magellan Telescope
HOL	High Order Low bandwidth
HPF	High-Pass Filter
LGS	Laser Guide Star
LIDAR	Light Detection And Ranging
LPF	Low–Pass Filter
LZT	Large Zenith Telescope
MF	Matched Filter
MOR	Moderate Order Radial
Na	Sodium
NCP	Non–Common Path errors
NFIRAOS	Narrow–Field–Infra–Red Adaptive Optics System
NGS	Natural Guide Star
OI	On–Instrument
RTC	Real–Time Computer
RTF	Rejection transfer function
SH	Shack–Hartmann
TMT	Thirty–Meter–Telescope
TT	Tip–Tilt
TWFS	Truth Wavefront Sensor
UVic	University of Victoria
WFS	Wavefront Sensor
ZO	Zoom Optics

ACKNOWLEDGEMENTS

I would like to thank Dr. Rodolphe Conan for making his knowledge of adaptive optics available to me and for providing guidance and insight for the duration of this work. I would like to thank my supervisor Dr. Colin Bradley for affording me the opportunity to contribute to such an exciting project.

I would also like to thank the other members of the University of Victoria Adaptive Optics Laboratory for making their expertise available to me when it was needed. In particular Dr. Peter Hampton for his help with control theory and Dr. Olivier Lardiere for his help and patience at the very beginning of this project.

Last but certainly not least, I would like to thank my family for their support, encouragement and interest.

For my parents, Lois and Ken Jackson,
who showed me what is possible.

Chapter 1

Introduction

Adaptive Optics (AO) is a correction technique which compensates for atmospheric turbulence. AO systems are currently in use by many existing research telescopes including the largest: the 10m-class telescopes. AO for large optical telescopes (30m-class) is currently under development; as the diameter of the telescope's primary mirror increases, so do the difficulties associated with providing good quality wavefront correction.

1.1 Thesis Organization

This thesis contains 6 chapters, beginning with a description of AO and an introduction to the issues faced in developing a system for an Extremely Large Telescope (ELT). In Chapter 2, a description of the AO system designed for the Thirty Meter Telescope (TMT) is presented as well as a framing of the particular issues for ELT AO that are addressed by this work. An outline of the modeling approach which is taken to solve those issues is given.

Chapter 3 introduces the control system of the TMT's AO system which has been designed to address some of the issues stated in Chapter 2. It contains an in-depth

description of the technical details of the model of the control system that has been developed. The equations which represent the components of the control system and the way in which they interact with each other within the model are given. Chapter 4 gives an overview of the experimental setup of the University of Victoria Laser Guide Star test bench which reproduces data as it will be collected by the wavefront sensors of NFIRAOS. Once the model was complete, the resulting control system was tested on the bench. Chapter 5 gives the results which indicate that the control system meets the requirements and solves the problems laid out in Chapter 2. Chapter 6 summarizes the conclusions and recommendations drawn from this work.

1.2 Extremely Large Telescopes

There are currently three ELT projects in various stages of development, all of which have a planned completion date for the year 2018. The European Southern Observatory (ESO) is designing the European ELT (E-ELT) which will be the largest of the three; its primary mirror will have a diameter of 42m and be composed of almost 1000 1.4m segments[1]. The Giant Magellan Telescope (GMT) will be the smallest of the three observatories at 24.5m and its primary light collecting surface will consist of 7 individual 8.4m segments, one of which has already been cast. The numerous partners include six American universities and institutions, the Australian National University, Astronomy Australia Ltd. and, most recently, the Korea Astronomy and Space Science Institute[2]. The TMT project intends to be the first of the ELTs to see first light: it is a public-private partnership between the Association of Canadian Universities for Research in Astronomy (ACURA), California Institute of Technology and the University of California. The TMT's primary mirror will consist of approximately 492 hexagonal segments, a depiction of the structure is shown in Fig. 1.1[3]. The

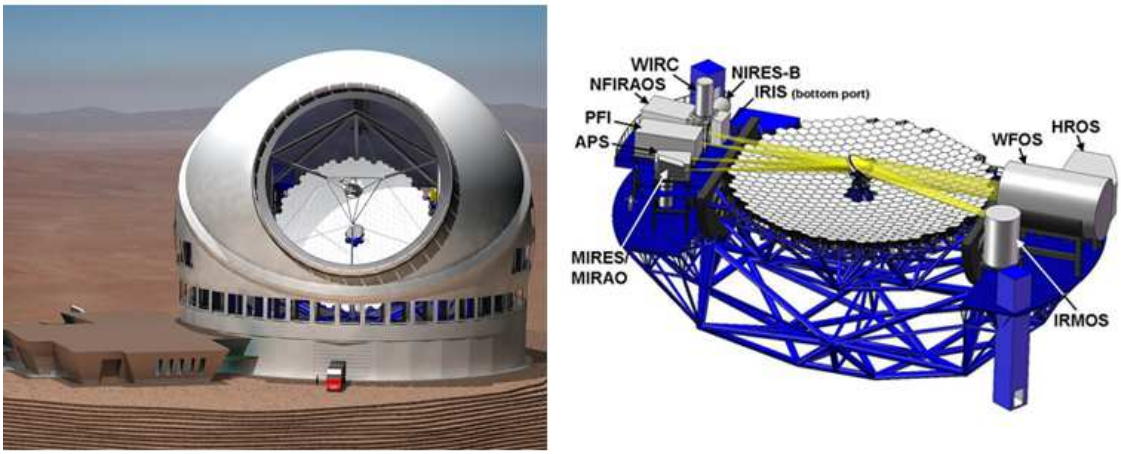

Figure 1.1: Depiction of the TMT dome structure (left) and primary mirror with instrument positions (right).

primary focus of this document will be the TMT and its AO system; the challenges related to AO for ELTs are generic; however, the solutions and studies described for mitigating these challenges are presented in the context of the TMT.

The construction of a thirty meter class telescope has been identified as one of the most important milestones in ground-based astronomy to be achieved in the first part of the 21st century [4]. There are four key science goals that the TMT and its instruments will be designed to achieve:

- Exploration of the "dark ages" - observation of first light objects in the universe
- Early formation of galaxies and large-scale structures
- The formation and effects of massive black holes on galaxy evolution
- Search for extra-solar planets, their properties and planet-formation processes

In addition to the science the TMT will be designed to do, the unknown discoveries yet to even be predicted are an equally strong motivation for constructing a next generation telescope such as the TMT, E-ELT and GMT. It is important to note that many of the science goals will not be achieved without a properly functioning

AO system which can correct incident wavefronts to near diffraction limited clarity. The sections below will outline the basics of adaptive optics and several of the key issues faced by all systems in addition to some problems unique to ELTs which, if unaccounted for, would cause a significant reduction in the system's performance.

1.3 Overview of Adaptive Optics

When light wavefronts from an astronomical object arrive at the Earth's atmosphere, they are effectively planar; theoretically, the resolution a telescope can achieve when focusing flat wavefronts is limited only by the diameter D of its entrance pupil and by the wavelength, λ, of the light being observed. It scales approximately as

$$\frac{1.22\lambda}{D}. \tag{1.1}$$

When the light passes through the atmosphere, however, the wavefronts become distorted due to turbulence which prevents ground-based telescopes from making diffraction limited images. The atmosphere is composed of pockets of air at different temperatures which are in constant motion. As the temperature and humidity of air changes, its index of refraction changes accordingly, thus each part of an incident wavefront is non-uniformly refracted multiple times upon passing though the atmosphere (see [5] for more on turbulence). The result is that an image taken by a ground-based telescope, although it may have a larger aperture than a space-based telescope, will have limited resolution and will be blurred. The goal of AO is to measure the distortion of the incident wavefronts and apply a corresponding corrective shape to a deformable mirror such that the distortions are cancelled and the wavefront again becomes flat.

There are three main components to an AO system: a Deformable Mirror (DM), a Wavefront Sensor (WFS) and a Real Time Computer (RTC). The layout of a

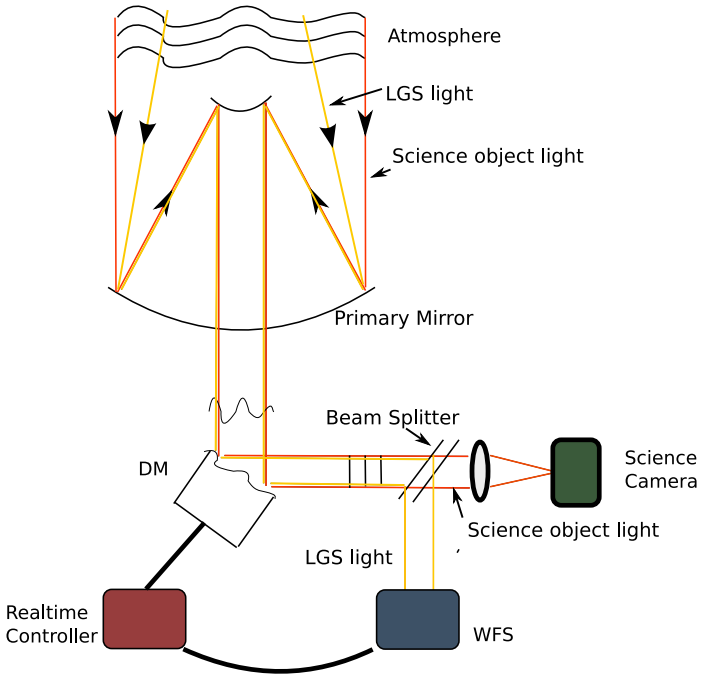

Figure 1.2: Schematic of closed loop adaptive optics.

generic closed loop system can be seen in Fig.1.2; the telescope is trained on two light sources, the science object and the reference source which is ideally a point source such as a star. Typically, each of these sources emit light in different wavelengths and the reference source falls in the visible spectrum while the science object falls in the infrared range. The light entering the telescope is directed to the (initially flat) DM; a beam splitter diverts the light from the reference source into the WFS which measures the shape of the wavefronts. The RTC uses the measurements to construct a command array of voltages to apply to the DM actuators such that the DM takes on a shape to cancel the wavefront distortions. The shape of the DM is continuously adjusted at a typical rate of about 1kHz to minimize the residual wavefront distortion. NFIRAOS will use Shack-Hartmann (SH) WFSs which provide information about the shape of the incident wavefronts by analysing the local slopes of individual segments of the wavefront, see Fig. 1.3. The main component is a 2-D lenslet array; the number and size of the lenslets determine the accuracy to which the

wavefronts can be reconstructed. Each lenslet focuses a spot onto the CCD and the X and Y position of that spot, relative to a reference position, indicates the magnitude and direction of the slope of that portion of the wavefront. The relationship between the spot displacement, d, and the wavefront slope, θ, is inversely proportional to the focal length, f, of the lenslets via the small angle approximation,

$$\theta = \frac{d}{f}. \tag{1.2}$$

A larger number of smaller lenslets corresponds to better detection of high spatial frequencies. A DM consists of a flexible reflective membrane laid over actuators which can be pushed or pulled using various mechanisms in order to change the shape of the mirror. Typically, the number of SH-WFS lenslets is equal to the number of DM actuators, and a higher number of closely spaced actuators allows better correction of high spatial frequencies. A DM having a greater number of actuators currently comes at the expense of speed and stroke, and as the order of the system (number of actuators/lenslets) increases, so does the amount of computation time taken by the control system to complete the wavefront reconstruction. DM technology is still evolving, with the goal of achieving fast, high stroke, high order DMs.

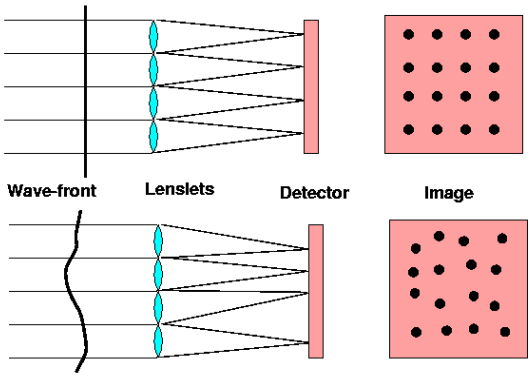

Figure 1.3: Shack-Hartmann WFS components

In an ideal system, the light wavefronts from the reference source will pass through exactly the same parts of the atmosphere as those from the science object; the two wavefronts will thus enter the telescope with the same shape. In a real system, it is standard to use a reference source located at a small angular distance from the science object. This introduces some error due to the difference in paths each wavefront travels through the atmosphere: the larger the angular separation, the greater the error. If the angular separation is too large, the reference source is outside the isoplanatic patch which is the area on the sky over which the atmosphere is sufficiently similar for AO correction to be effective. There are two types of reference sources: Natural Guide Stars (NGSs) and artificial guide stars generated by exciting particles in the atmosphere using a laser beacon, also called Laser Guide Stars (LGSs). Sodium LGSs will be used by the TMT and are discussed in Sec. 1.4.1.

In an NGS AO system no laser beacon is required and the reference is a true point source located effectively at infinity. The main drawback of an NGS is that there is a system dependent upper limit on the magnitude of the guide star (N.B. higher magnitude corresponds to a lower intensity). The sky coverage is therefore limited to the isoplanatic patch surrounding each available guide star and it is left to chance whether or not a suitable guide star will be located within the isoplanatic patch around any given science object being observed. To address this limitation, many AO systems generate an artificial reference source. An LGS can be pointed to any position on sky that the telescope can point, and therefore can increase a telescope's sky coverage significantly. Use of an LGS AO system does not increase sky coverage to 100%. Because the laser light travels both up and down through the atmosphere in a very short time, distortions due to atmospheric tip/tilt are cancelled by the return trip. As tip and tilt are far from negligible, a means to detect their magnitude is necessary. This is done by use of an NGS; however, the limits on magnitude and

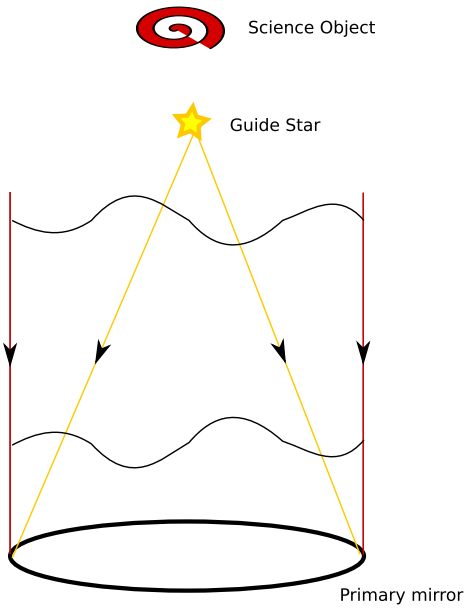

Figure 1.4: The cone effect

proximity to the science object are much less restrictive and the sky coverage can by greatly increased.

The use of an LGS moves the reference source from infinity to approximately 90km above the telescope (in the case of an Na LGS). This means that the light no longer travels through a column of the atmosphere as does the light from the science object, but is generated in the upper atmosphere and enters the telescope as an expanding cone (Fig. 1.4). The result is that the reference light does not travel through all of the turbulence experienced by the science light which means that some aberrations can not be corrected. This effect is minimized by use of multiple guide stars arranged in an asterism within the FOV.

1.4 LGS AO for ELTs

For the TMT, a strictly NGS AO system would limit the sky coverage to approximately 2% at the galactic pole for correction in the near infrared [6]. It has been

identified as a science requirement that a minimum sky coverage of 50% at the galactic pole must be achieved for the AO facility [7]. The direction of the galactic pole has the fewest candidate guide stars and will therefore yield the worst sky coverage. The only way to meet this science requirement is to use an LGS AO system. This will meet the sky coverage requirement; however, it will introduce sources of error in addition to those described above which have not been required to be addressed by existing AO systems. These error sources are due to the large diameter of the TMT and must be overcome in order to achieve high quality correction[8]. The main issues to be addressed by this work are the direct result of the physical properties of the atmospheric sodium layer.

1.4.1 Atmospheric Sodium Layer

A layer of sodium (Na) atoms exists in Earth's atmosphere at a mean altitude of 90km with a mean thickness of 10km, see Fig. 1.5[9]. An LGS is generated by shining a 589nm Na laser at this layer to excite the Na atoms. The atoms emit light as they return to ground state, thus creating a beacon. The distribution of sodium atoms within the layer is neither uniform, nor static. It varies with altitude and fluctuates over time. This means that the altitude of the layer is not stationary at 90km, the thickness is not fixed at 10km and the vertical profile changes constantly.

1.4.2 WFS Spot Elongation

These properties of the sodium layer, coupled with the large diameter of an ELT's primary mirror, will cause the system to measure a wavefront aberration which is not due to atmospheric turbulence. This could be a significant source of error for an ELT's AO system if unaccounted for. The physical dimensions of the Na layer have a particularly strong effect on AO for ELTs because of the geometry of the system

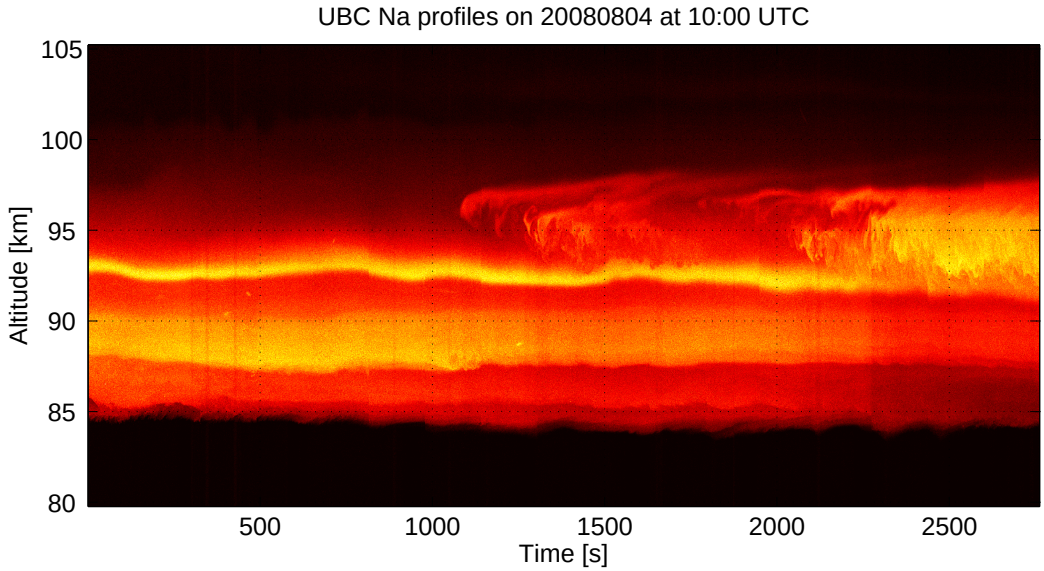

Figure 1.5: LIDAR of atmospheric sodium layer. Pixel colours range from dark to light showing lower to higher atom density, respectively.

which is illustrated in Fig. 1.6[10]; the large diameter of the primary mirror means that the lenslets positioned at the edge of the WFS will observe the LGS from several meters off-axis from the laser launch point. As a result, the LGS no longer appears as a point source on the lenslets of the WFS. The column of light emitted by the excited Na atoms starts to become visible and the WFS will measure radially elongated spots whose lengths increase with the distance of a lenslet off-axis from the laser launch point. In the case of the TMT, the maximum elongation at a radius of 15m for a 10km thick sodium layer centred at an altitude of 90km will be almost 4 arcsecs which will be 8 pixels on the LGS WFS CCD. Consequently, the change in mean altitude, layer thickness and density distribution will all be detected by the WFS. This implies that in the absence of atmospheric turbulence, use of an LGS as a reference for an ELT will result in a non-zero, non-negligible phase aberration measurement from the WFS due to the WFS spot elongation and the Na layer fluctuations which are now visible to the system.

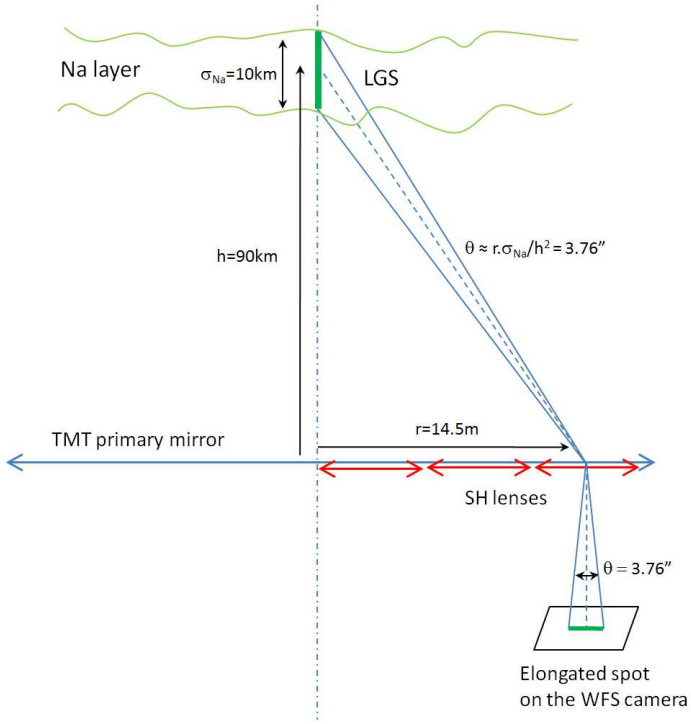

Figure 1.6: Perspective effect due to the diameter of the primary mirror and the thickness of the sodium layer.

Chapter 2

The Narrow Field Infrared Adaptive Optics System

2.1 Overview of NFIRAOS

In light of the effects of the Na layer properties presented in Sec. 1.4, a specially designed AO system must be constructed for the TMT. The Narrow Field Infrared Adaptive Optics System (NFIRAOS) will be the TMT's first light facility adaptive optics system and will reside on one of the telescope's Nasmyth platforms[11],[12],[13] (Fig. 2.2)[3]. It will eventually provide near diffraction limited correction for three proposed science instruments: a near IR integral field imaging spectrograph, a near IR echelle spectrograph and a wide field IR camera. It will be required to correct over the wavelength range of 1.0-2.5 microns. NFIRAOS will be a Multiconjugate AO (MCAO) system using 2 DMs. One DM will be a 60x60 actuator ground-conjugated DM with a 300 mm pupil and a stroke of no less than 9 microns. The second DM will be conjugated to 12km, have 72x72 actuators and a 360 mm pupil. The system will eventually be upgraded and the ground-conjugated DM will have 120x120 actuators

with a smaller stroke. To compensate for this smaller stroke, ($< 3\mu m$) the telescope secondary mirror will be replaced by an adaptive secondary to act as a "woofer" by providing larger amplitude, low spatial frequency corrections [12].

NFIRAOS will employ 6 LGSs in order to mitigate the cone effect (Sec. 1.3); each guide star will be detected by a 60x60 SH-WFS (120x120 after upgrading) at a frame rate of 800Hz. The LGSs will be generated by a 100W, 589nm sodium laser and launched from the rear side of the TMT's secondary mirror. The LGSs are launched from the top of the telescope to form a 70 arcsec diameter pentagonal asterism with one central guide star. The FOV requirement is 30 arcsecs, though it will initially correct a 10 arcsec science field[13]. NGSs will be used to provide data to the Truth WFSs. The first, called the On-Instrument WFS (OI-TTF-WFS), will track the atmospheric tip/tilt and focus aberrations and be detected by a 2x2 SH-WFS. The framerate of this WFS will fall in the range of $100 - 800$ Hz. The exact framerate will be selected based on the magnitude of the guide star used for a given observation. The slower framerate corresponds to a higher magnitude star. This variable framerate will be necessary in order to maintain a minimum SNR to maintain a high level of correction, ensuring the whole system remains within the error budget. The second WFS, called the Medium Order Radial Truth WFS (MOR-TWFS), will be a 12x12 SH-WFS and will track the slower changes in the medium order Zernike modes of the atmospheric turbulence. The MOR-TWFS will, therefore, provide periodic updates to the DM shape at a rate in the $0.1 - 5$ Hz range which will also be selected based on the magnitude of the guide star being observed. A third WFS, the High-Order Low bandwidth Truth WFS (HOL-TWFS), will operate at a very slow frame rate and will be a 120x120 SH-WFS. The HOL-TWFS will provide periodic corrections to the mirror shape with the goal of reducing any significant build up of high order, slowly changing shapes on the DM which will be undetected by the other WFSs.

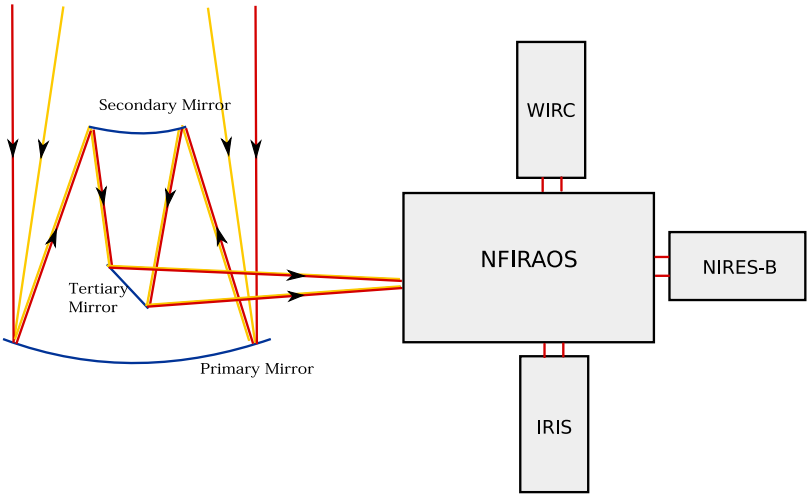

Figure 2.1: Top level light path from telescope mirrors to NFIRAOS to science instruments.

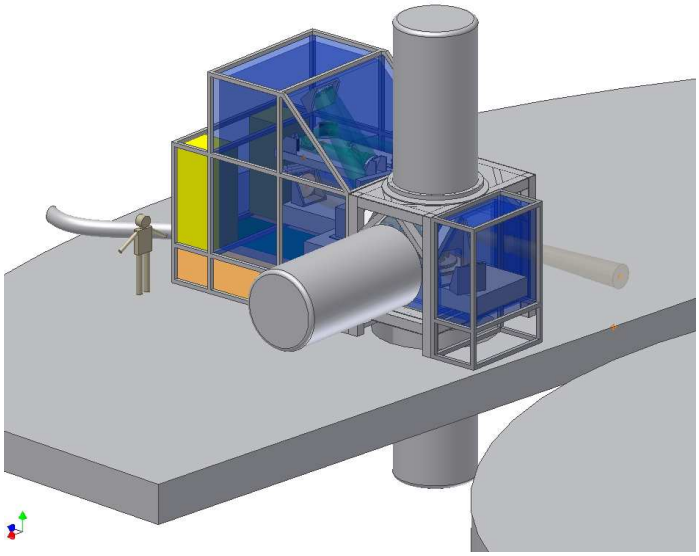

Figure 2.2: Rendering of NFIRAOS on the Nasmyth platform.

2.2 Project Motivation

As outlined in Chapter 1, several issues must be addressed in order to develop an effective AO system for an ELT. (Not all of the issues will be addressed in this work). The main focus is an effort to overcome the problem of elongated LGS spots and the resulting effects induced by the properties of the sodium layer. The purpose of this work is to verify the performance of a centroiding algorithm, called the *constrained matched filter*[14]. The algorithm must effectively prevent corruption of the science path induced by the dynamic sodium layer. It must also work within the control system of NFIRAOS's Real Time Computer (RTC) which will process input information from multiple WFSs at multiple rates while maintaining stable closed loop correction. This work has taken a control system designed specifically [7] to use the matched filter algorithm and implemented that system in simulation in order to characterize and sugest changes which improve its performance.

2.2.1 Description of the Matched Filter Method

The main reasons that the constrained matched filter (described in [14]) was chosen as the centroiding algorithm for detection of LGS WFS spot positions in NFIRAOS are twofold:

- The matched filter is effective even when photon flux is low.
- Its linear range can be extended.

The first point is important for accurate measurements of the elongated spots toward the edge of the LGS WFSs as the photons will be spread over an increasing number of pixels with distance off-axis, decreasing the SNR of the outer lenslets in an environment which is already quite photon-starved. Regarding the linear range, in practice it has been found that the matched filter is linear for very small pixel

displacement; however, it can be constrained such that the linear range is extended [15]. This means that, for a spot shifted a given distance on its lenslet, a constrained matched filter will be able to measure acurately that position for a larger amount of shift than the unconstrained version.

The matched filter is based on a first order Taylor expansion of shifted spot image $I(\theta_x, \theta_y)$,

$$I(\theta_x, \theta_y) = I(0) + \theta_x \frac{\partial I}{\partial \theta_x} + \theta_y \frac{\partial I}{\partial \theta_y}. \tag{2.1}$$

$I(0)$ is the un–shifted spot images and $\frac{\partial I}{\partial \theta_x}$, $\frac{\partial I}{\partial \theta_y}$ are the spot derivatives. The underlying assumption is that the atmospheric turbulence affects only the fast motion of the spot θ_x and θ_y leaving un–changed the spot pattern $I(0)$ whereas the varying Na profile also modifies the spot pattern $I(0)$ and induces slow spot drifts. The matched filter then requires the knowledge of the spot pattern $I(0)$ and of the spot x and y derivatives. Knowledge of this information leads to values referred to as the *Offset* and *Gain*, respectively. The offset is a reference position which sets the zero-point of each subaperture and is determined by calculating the centroids of the spots in $I(0)$.

$I(0)$ can be deduced from a time average of snapshot spots I; the time average has to be long enough to smooth out the turbulence effects but shorter than the typical time scale of Na density fluctuations.

Eq. (2.1) can be re–written using the following notation

$$I - I_0 = G\boldsymbol{\theta} \tag{2.2}$$

where I is a column vector which contains a snapshot spot image from one WFS lenslet in raster format, $I_0 = I(0)$ is also a column vector of the same size as I which contains a time averaged spot image from the same lenslet in raster format. G is a matrix whose two columns contain the x and y derivatives of I and $\boldsymbol{\theta}$ is the column

vector of wavefront gradients. G is usually called the matrix of pixel gains, or simply the matched filter gain. Taking the pseudo–inverse R of G, $R = (G^T G)^{-1} G^T$ leads to $\boldsymbol{\theta}$

$$\boldsymbol{\theta} = R(I - I_0). \tag{2.3}$$

R is what is called the matched filter. This calculation is repeated for each spot on the WFS image. The noise–weighted constrained matched filter which has been derived to extend the linearity to the range ± 1 pixel can be found in [14] and [15]; the practical derivation and implementation of the constrained matched filter is given in section 3.1.3.

The so-called gain is the rate of change in intensity of a pixel with respect to spot motion. Therefore, if a known motion is applied to the guide star position it is possible to calculate this rate of change. The known motion is referred to as a *Dither Signal* and it will be generated by using a tip/tilt mirror, called the Fast Steering Mirror (FSM), to move the position of the LGS beacon on-sky. The shape of the dither signal is optional; NFIRAOS will use a circular shape generated at 200Hz and sampled at four points per dither cycle (800Hz) resulting in a diamond shaped pattern (Fig. 2.3).

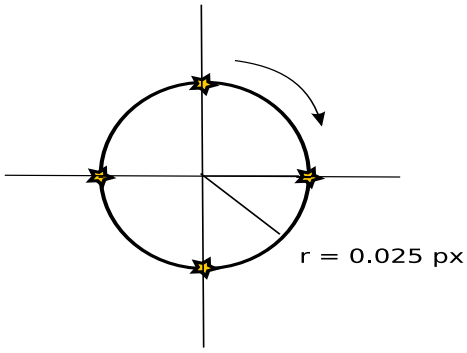

Figure 2.3: Dither signal shape and the points at which measurements are taken.

The difference in spot intensities, from measurements taken at opposite vertices

of the diamond, is divided by the diameter of the dither signal circle to obtain the gain. Because the sodium layer is dynamic, the matched filter gain and offset must be periodically recalculated in order to avoid degradation in its performance. However, atmospheric turbulence is present in all measurements and so the time average must be both long enough to smooth out the turbulence effects but also short enough such that the Na density fluctuations are not obscured. Similarly, the set of four images used to calculate the gain are accumulated over many dither periods and averaged at each position before carrying out the calculation. A more in-depth discussion of the approach used to measure the gain and offset within the simulation is presented in Chapter 3.

2.3 Modeling the NFIRAOS Control System

A simulation will be developed which will implement the control system outlined in the NFIRAOS RTC algorithm description [7]. The simulation will be developed in the Matlab Simulink environment and will build on previously completed work which showed first that a representation of the dynamic sodium layer could be simulated in the form of a single elongated spot [16], and then, that the matched filter could remain stable in closed loop in a noise and turbulence free environment while measuring and rejecting the dynamic properties of the sodium layer [17]. The simulation will implement models of the hardware including the DM, FSM, LGS WFS, Truth WFSs, and zoom optics. It will simulate atmospheric turbulence in the form of phase aberrations and apply it to the input data which will be sodium profiles for the LGS WFS and point sources for the NGS WFSs. The sodium profiles were obtained from the Large Zenith Telescope[9]. Specific issues considered when developing the simulation include the following:

- The matched filter must be recalculated or updated at regular intervals while NFIRAOS is running.
- Wavefront correction calculated in the form of a shape applied to the DM will require the combination of input data from various sources at different rates.
- NGS magnitudes will not be constant.
- The mean altitude of the sodium layer must be tracked to prevent large focus errors.
- The FSM will be used both to dither the LGS on sky and to stabilize it against windshake and vibrations.
- Any delay between laser launch and detection of the LGS light (ex. travel time) must be measured or estimated.
- The system must converge within 20 seconds once the loop is closed.

The matched filter is updated to prevent changes in the LGS due to temporal variation in the sodium layer atom density distribution from corrupting the science path. In addition to exploring the effects of combining multi-rate data, the effects of changes in those rates with respect to each other will be evaluated. The proposed control architecture [7] will be implemented in simulation as near as possible to the original specifications; modifications to this design will be tested and recommended as instabilities and their sources are identified. An overview of the proposed system and a complete description of the resulting simulation will be presented in Chapter 3.

The UVic AO Lab has at its disposal a highly developed AO Matlab toolbox[18]. It will be used to simulate the hardware components listed in Sec. 2.3. Once the

simulation is completed, its performance will be evaluated in the context of the performance requirements. It will first be tested for long term stability; if instability occurs, the system will be adjusted and recommendations for changes will be noted. The performance of the matched filter will be validated by comparing the system response when the Na layer input data is static to the response to a dynamic Na input with the expectation that there will be little degradation of performance for a dynamic sodium layer. In order to gain an understanding of the effects of certain parameters such as gain values and frame rates, an analytical model will be developed and its predictions compared to the performance of the simulation. This will be used to help narrow some of the parameter ranges for stable performance. Finally, the simulation will be ported to the UVic LGS test bench which will implement the control system using real hardware and input data. If the control and data processing executed in simulation can be shown to be stable and provide good correction on a real system, it will be considered a success.

Chapter 3

Simulink Model of NFIRAOS

In this chapter, the various processes and control loops implemented by the NFIRAOS simulation are described. The equations used to construct the simulation are given. Where possible, their Simulink implementations within the model are also shown. There are five main paths, three of which contribute directly to the closed loop control of the DM via different WFSs; these are the paths highlighted in green and pink and the unhighlighted path in Fig. 3. The fourth path is highlighted in orange and provides slow tip/tilt and focus feedback from the LGS WFS to the FSM and zoom optics, respectively, and the fifth, highlighted in purple, outlines the slowest background processes required to periodically provide updated matched filters in order to maintain accurate measurements from the LGS WFS.

3.1 Background Tasks

The computations executed at a much slower rate than the closed loop LGS correction rate of 800Hz are called background tasks. These processes monitor slow changes in the Na profile and provide periodic updates to the system to prevent the slow changes from corrupting the science image.

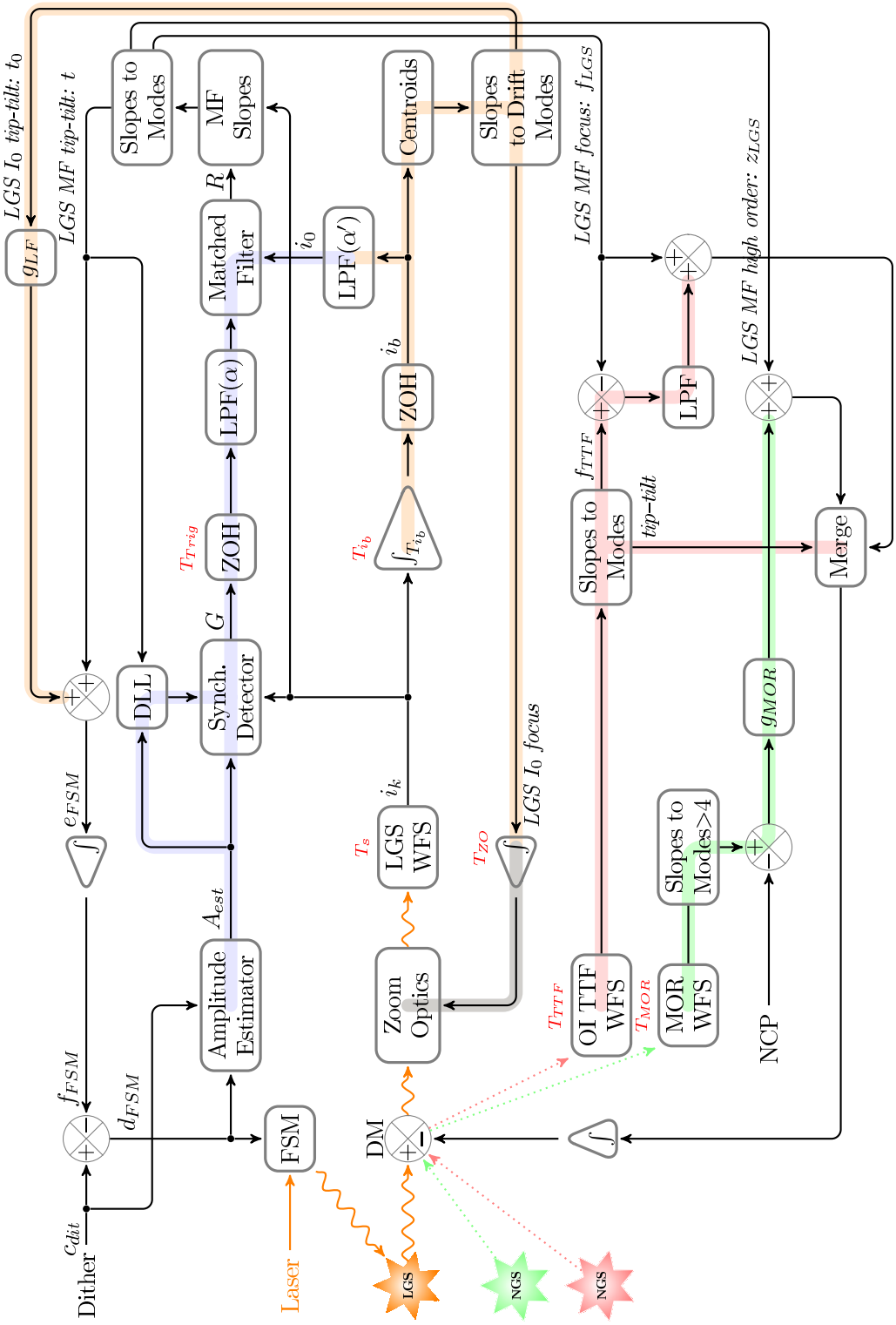

Figure 3.1: Block diagram of NFIRAOS LGS wavefront sensing control system.

3.1.1 Gain Estimation

As stated in Sec. 2.2.1, in order to maintain an accurate matched filter based on the most recent sodium layer information, new offsets and gains are determined periodically and the values are used to update the matched filter. The purple path in Fig. 3 indicates the process followed by the simulation for estimating the matched filter gain. The method requires that a dither signal be added to the FSM motion in order to induce a known motion of the LGS on-sky. The dither signal is a circular motion of radius $A = 0.025$ pixels sampled at $\frac{1}{T_x} = \frac{1}{n_d T_s}$ =200Hz, where $n_d = 4$, and $\frac{1}{T_s} = 800Hz$ is the RTC frame rate. It is generated in the simulation by offset sinusoids of equal amplitude and period,

$$c_{dit_x} = Asin(2\pi k/n_d) \tag{3.1}$$

$$c_{dit_y} = Acos(2\pi k/n_d). \tag{3.2}$$

The Simulink implementation of the dither signal generation, described by Eqs. 3.1 and 3.2, is shown in Fig. 3.2.

Delay Locked Loop

The dither signal defined by Eqs. 3.1 and 3.2 allows straightforward estimation of the gain, G, provided the system delay is known. The delay locked loop compares the tip/tilt values, $\mathbf{t}(k)$, measured by the LGS WFS at 800Hz, to a reference signal and determines the system phase delay. Phase errors, Δ_m, in the dither signal measurements are accumulated as follows:

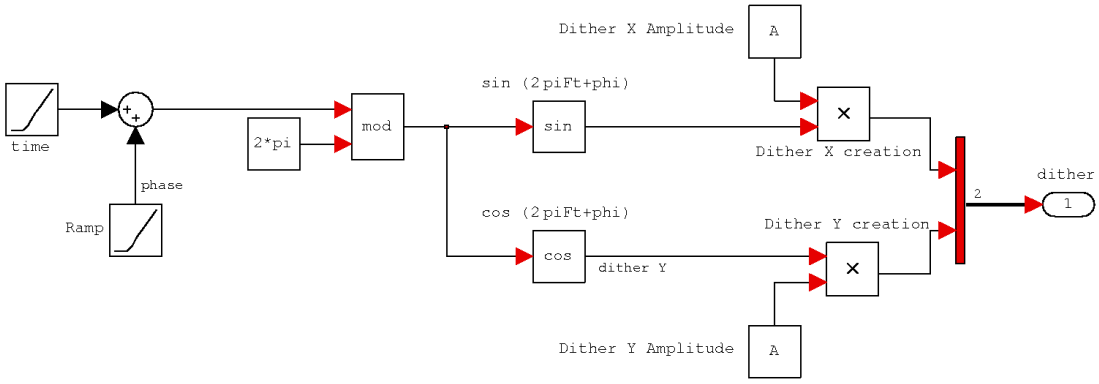

Figure 3.2: Simulink implementation of dither signal generation.

$$\delta(k) = \delta(k-1) + \frac{g_{dll}}{A_{EST}}[cos(2\pi k/n_d + \Delta_{m-1})t_x(k) - sin(2\pi k/n_d + \Delta_{m-1})t_y(k)], \quad (3.3)$$

and

$$\Delta_m = \delta(k) \text{ if } \frac{k}{n_d n_{dll}} = m. \quad (3.4)$$

The rate of the DLL is expressed as $\frac{1}{T_{dll}} = \frac{1}{n_d n_{dll} T_s}$ where n_d is the number of RTC frames per dither period and n_{dll} is an integer number of dither periods (the minimum value of n_{dll} is one). The loop gain, g_{dll}, is the ratio of the RTC frame rate to the DLL frame rate, T_s/T_{dll}; and both $t_x(k)$ and $t_y(k)$ are normalized by division by the estimated dither amplitude A_{est}. In order to reduce the time needed to converge to an accurate phase measurement at the beginning of the run, an initial condition, $\delta(0)$, is used. This is an estimated value of the total system delay. A look-up table can be constructed for this parameter if all major causes of phase delay can be characterized.

The major factors identified so far are the round-trip travel time of the laser light as a function of telescope zenith angle and the gain of the FSM closed loop integrator. In order to verify the performance of the DLL in the simulation, a scalar model with a single integrator was implemented and the relationship between the integrator gain and the measured phase delay was noted. The phase shift induced by the FSM closed–loop was found to vary approximately linearly between 0 and $\pi/4$ as the the FSM integrator gain was varied from 0 to 1. The FSM delays were independent of zenith angle (i.e. input delay of the dither signal). Using this relation and the known round trip delay, applied directly to the sinusoid generated for the creation of the dither signal, it was possible to accurately predict the value measured by the DLL in the full NFIRAOS simulation for a given FSM gain and zenith angle. This indicates that there are no other significant sources of phase delay generated in the simulation and the DLL is behaving as expected.

Previously, the DLL was configured such that a second integrator, Eq. 3.5,

$$\Delta_m = g_{dll'}\delta(k) + \Delta_{m-1} \text{ if } \frac{k}{n_d n_{c'}} = m \tag{3.5}$$

periodically summed the output of the accumulator described by Eq. 3.3. It was found that the system was stable only when $n_{c'} = n_c$, the integer number of dither periods used to calculate a new matched filter. The resulting phase measurement was accurate for a constant phase delay; however, for a changing delay the DLL was very slow due to the long period of the background tasks. The integrator was removed and Eq. 3.5 rewritten as follows,

$$\Delta_m = \delta(k). \text{ if } \frac{k}{n_d n_{dll}} = m \tag{3.6}$$

where the minimum value of n_{dll} is one (i.e. updated every dither period, n_d). The

predictability was tested for various constant input delays and FSM gains, and the results were found to be as accurate as those of the previous configuration. A ramp input delay was implemented and the measured phase ramp values, for any given time step, were within 0.05 radians of the predicted values when the model was run for 30 seconds (simulation time). It was also observed that the phase measurement converged to within 0.1 radian of the predicted value when the FSM gain was changed abruptly in the middle of the simulation. The stability of the system is not disrupted when $n_{dll} \neq n_c$. In all tests, the Na profiles were changing, readout and photon noise was present and atmospheric turbulence was changing with time. The Simulink implementation of the DLL is shown in Fig. 3.3.

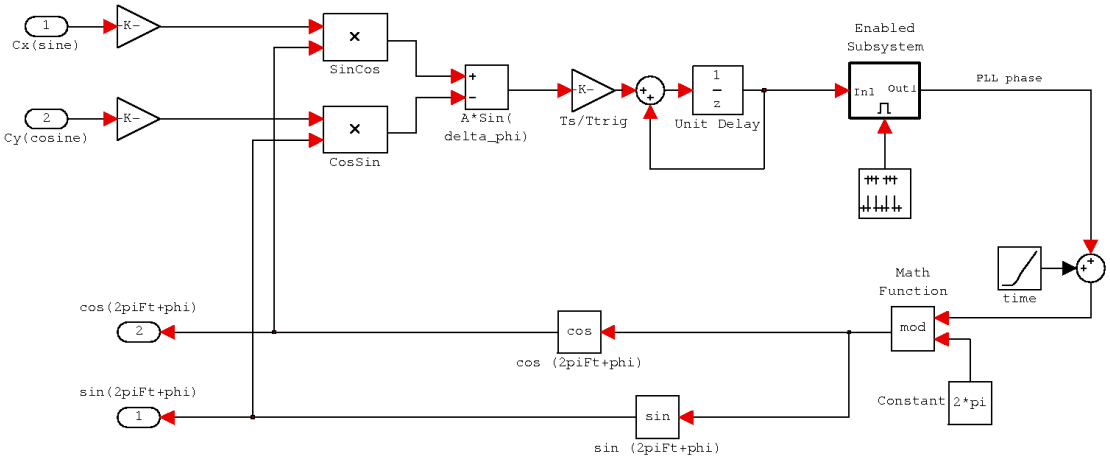

Figure 3.3: Simulink implementation of the delay locked loop.

Amplitude Estimation

In order to measure the system delay, the measured LGS tip and tilt, $t_x(k)$ and $t_y(k)$, must be normalized by the actual dither signal amplitude (Eq. 3.3). Tip/tilt data from the LGS WFS measurements is used to generate a tip/tilt feedback vector, e_{FSM}, which is used to stabilize the position of the LGS on-sky (see Sec. 3.2).

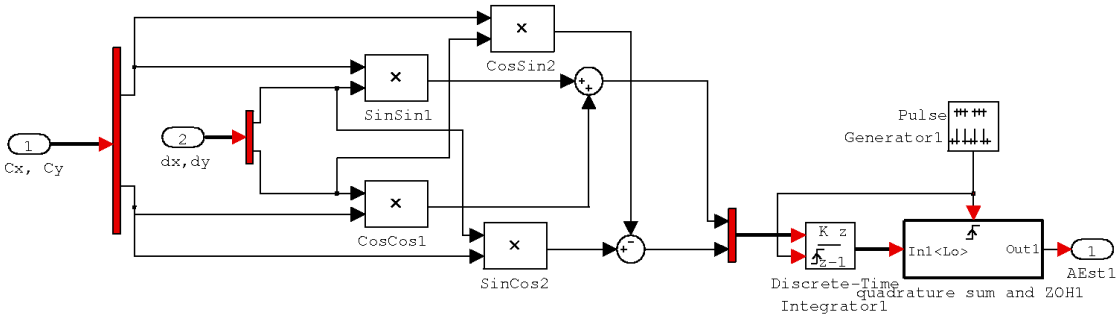

Figure 3.4: Simulink implementation of amplitude estimation subsystem.

The injected dither signal is summed with this feedback vector to generate the FSM commands. This feedback loop will cause a small change in the actual amplitude of the dithering motion of the LGS which will, therefore, need to be estimated. The correlations between the injected dither signals, (c_{dit_x}, c_{dit_y}), and the FSM commands, (d_{FSM_x}, d_{FSM_y}), are averaged over n_c dither periods, and summed in quadrature to obtain the amplitude estimate, A_{est}.

$$(ip)_q = \sum_{k=(q-1)n_d n_c+1}^{qn_d n_c} d_{FSM_x}(k)c_{dit_x}(k) + d_{FSM_y}(k)c_{dit_y}(k) \tag{3.7}$$

$$(qd)_q = \sum_{k=(q-1)n_d n_c+1}^{qn_d n_c} d_{FSM_x}(k)c_{dit_y}(k) - d_{FSM_y}(k)c_{dit_x}(k) \tag{3.8}$$

$$(A_{est})_q = \frac{1}{n_d n_c A}\left[(ip)_q^2 + (qd)_q^2\right]^{1/2}, \tag{3.9}$$

where q denotes the time index of the current dither amplitude estimate and ip, qd are respectively the in-phase and quadrature components of the FSM motions.

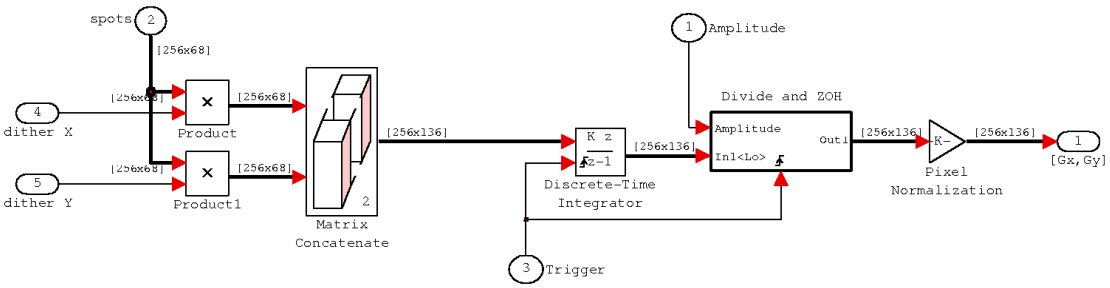

Figure 3.5: Simulink implementation of the synchronous detector.

Synchronous Detector

Once the amplitude estimate, A_{est}, and the phase compensated LGS tip/tilt measurements, Δ_m, from the DLL are obtained, they are used by the synchronous detector to determine the gains by taking the partial derivative of intensity on pixel j of the boxcar averaged image, i_b, with respect to spot displacement, θ, on the subaperture. This correlation between injected signal and pixel intensities is averaged over n_c dither cycles, thus generating the q^{th} boxcar average estimate of the gain matrix, G.

$$\left(\frac{\partial i_b(j)}{\partial \theta_x}\right)_q = \frac{2}{A_{est} n_d n_c} \sum_{k=(q-1)n_d n_c+1}^{q n_d n_c} sin(2\pi k/n_d + \Delta_{m-1}) i_k(j) \tag{3.10}$$

$$\left(\frac{\partial i_b(j)}{\partial \theta_y}\right)_q = \frac{2}{A_{est} n_d n_c} \sum_{k=(q-1)n_d n_c+1}^{q n_d n_c} cos(2\pi k/n_d + \Delta_{m-1}) i_k(j) \tag{3.11}$$

The output signal is held for n_c dither cycles, or one so called matched filter update period T_{trig}. The rate, $\frac{1}{T_{trig}} = \frac{1}{n_d n_c T_s}$Hz, will be in the range of 0.1 to 10 Hz. A low pass filter is applied in order to smooth the change in the matched filter matrix,

$$\left(\frac{\partial i_0(j)}{\partial \theta}\right)_q = \alpha \left(\frac{\partial i_0(j)}{\partial \theta}\right)_{q-1} + (1-\alpha)\left(\frac{\partial i_b(j)}{\partial \theta}\right)_q . \tag{3.12}$$

3.1.2 Offset

The second input required to calculate a matched filter is a reference or offset; the beginning of the orange path on Fig. 3 executes the following: the boxcar averaged intensity vector i_b is accumulated over $n_{c"}$ dither periods,

$$(i_b)_v = \frac{1}{n_d n_{c"}} \sum_{k=(v-1)n_d n_{c"}+1}^{q n_d n_{c"}} i_k, \tag{3.13}$$

i_b is then low pass filtered to obtain the reference intensity vector i_0. Note that the rate at which the synchronous detector calculates a new gain estimate ($\frac{1}{n_d n_c T_s}$) and the rate at which the reference vector is calculated ($\frac{1}{n_d n_{c"} T_s}$) are not constrained to be equal. It is proposed that several other processes, which also depend on the average intensity vector, i_b, have shorter time constants in order to improve their performance. To increase the frequency at which the boxcar average i_b is triggered, without changing the overall time constant of the transfer function of i_0 with respect to that of the gain estimate, G, the coefficient of the gain estimate low pass filter described by Eq. 3.12 must be adjusted before being applied to i_b. The rate of the trigger of i_b is $\frac{1}{T_{i_b}} = \frac{1}{n_d n_{c''} T_s}$Hz, where $n_{c''} \leq n_c$ is also an integer number of dither periods. The new coefficient, α' will be a function of T_{trig}, T_{i_b} and the original coefficient, α.

$$(i_0)_v = \alpha'(i_0)_{v-1} + (1-\alpha')(i_b)_v \tag{3.14}$$

The coefficient α' is adjusted as follows: $G(z)$ is the transfer function of the LPF in Eq. 3.12,

$$G(z) = \frac{1-\alpha}{1-\alpha z^{-1}}. \tag{3.15}$$

$G(z)$ can be expressed in terms of its sampling period,

$$G_{sample}(z) = \frac{1 - e^{-aT_1}}{1 - e^{-aT_1}z^{-1}}. \tag{3.16}$$

Equating the coefficients of the z^{-1} terms yields an expression for a in terms of α,

$$e^{-aT_1} = \alpha \tag{3.17}$$

$$a = \frac{-log(\alpha)}{T_1} \tag{3.18}$$

$$T_1 = T_{trig}. \tag{3.19}$$

If a new sampling time, T_{i_b}, is introduced for the i_b update, the coefficient a must remain the same, thus the new coefficient, α' of the LPF must be determined as a function of α and the ratio of the two sampling rates.

$$e^{-aT_2} = \alpha' \tag{3.20}$$

$$e^{-\frac{-log(\alpha)}{T_1}T_2} = \alpha' \tag{3.21}$$

$$\alpha^{T_2/T_1} = \alpha' \tag{3.22}$$

$$T_2 = T_{i_b}. \tag{3.23}$$

Thus Eq. 3.14 becomes,

$$(i_0)_v = \alpha^{T_{i_b}/T_{trig}}(i_0)_{v-1} + (1 - \alpha^{T_{i_b}/T_{trig}})(i_b)_v. \tag{3.24}$$

3.1.3 Matched Filter Algorithm

In the framework of Shack–Hartmann wavefront sensing, matched filtering refers to noise-weighted least-squares estimation of subaperture spot displacements from detector pixel intensities[14]. A measured pixel intensity vector in each subaperture, i_{model}, is modeled as

$$i_{model} = i_0 + G\theta + \eta, \tag{3.25}$$

where i_0 and G are as described above (Sec. 3.1.1 and Sec. 3.1.2), θ is the displacement on each subaperture and η is the measurement noise. Readout noise and photon noise are both accounted for in the simulation . To get an estimate, $\hat{\theta}$, of the image displacement, the problem must be inverted resulting in the following expression:

$$\hat{\theta} = Ri \tag{3.26}$$

where R is a constrained matched filter and is derived from the gain matrix G, the offset i_0, the noise covariance matrix C_η, and a constraints matrix M.

$$R = M(\tilde{G}^T C_\eta^{-1} \tilde{G})^{-1} \tilde{G}^T C_\eta^{-1} \tag{3.27}$$

where

$$\tilde{G} = [G \mid i_0 \mid i_1 \mid i_2 \mid i_3 \mid i_4], \tag{3.28}$$

$$M = \begin{bmatrix} 1 & 0 & 0 & 1 & -1 & 0 & 0 \\ 0 & 1 & 0 & 0 & 0 & 1 & -1 \end{bmatrix} \tag{3.29}$$

and

$$C_{\eta}^{-1} = diag[1/(\sigma_E^2 + i_0)] \tag{3.30}$$

The vectors i_j for $1 \leq j \leq 4$ in Eq. 3.28 are copies of the reference spot image, i_0, shifted by ± 1 pixel in both the x and y directions, and σ_E in Eq. 3.30 is the readout noise. The constraints matrix is derived from the following conditions implemented to improve the range of linearity:

- $R \cdot G = I$, where I is a 2x2 identity matrix,
- $R \cdot i_0 = 0$, the reference position corresponds to zero displacement,
- $R \cdot i_j = 1$, the estimated $\hat{\theta}$ of an image shifted by $\pm$ 1 pixel in x or y will be exactly 1 pixel.

Using the estimates of offset and gains obtained by the methods described above, the q^{th} matched filter, R_q, is calculated at the selected background rate of T_{trig}. R_q is applied at 800Hz to the current LGS WFS image to obtain the wavefront slopes,

$$\hat{\theta} = R_q \cdot i. \tag{3.31}$$

3.1.4 Computation of LGS WFS Drift Modes

The rest of the path highlighted in orange in Fig. 3 shows the computation and utilization of the LGS WFS drift modes, values which must be periodically updated. Each time a new average intensity vector, i_b, is computed, the slopes are determined by a center of gravity computation. These slopes are then used to project the tip/tilt and focus (Z_2, Z_3, Z_4) Zernike coefficients from i_b which contribute to the FSM commands and drive the zoom optics respectively. Due to the high pass filter nature of the matched filter centroiding algorithm, slow changes are not measured, thus the

slow changes in the sodium layer are distinguished and removed from the closed loop correction of turbulence induced wavefront error.

Drift focus

In the case of the focus it is advantageous to track the changes in the sodium layer mean altitude as this is the altitude at which the LGS WFS is to be focused. The focus, f_b, measured from each new i_b is integrated at $1/T_{zo} = 100Hz$,

$$f_{zo}(k) = g_{zo} f_b(k) + f_{zo}(k-1), \tag{3.32}$$

and the physical motion of the lenses driven by the zoom optics motor is represented by a discrete 1Hz low pass filter with the following transfer function,

$$G_{zo}(z) = \frac{1 - e^{-2\pi T_{zo}}}{1 - e^{-2\pi T_{zo}} z^{-1}}. \tag{3.33}$$

Drift Tip/Tilt

As in the case of the focus measured by the LGS WFS, slow tip/tilt is not sensed due to the HPF applied by the matched filter. The tip/tilt drift must be monitored in order to identify disturbances such as windshake. These drift modes, $t_0(k)$, are resampled at 800Hz, scaled by a gain g_{LF}, and combined with the LGS WFS tip/tilt modes, $t(k)$,

$$e_{FSM} = g_{LF} t_0(k) + t(k), \tag{3.34}$$

to create the FSM tip/tilt feedback vector e_{FSM}. Thus the LGS position on-sky is stabilized. The FSM feedback is a part of the unhighlighted 800Hz path in Fig. 3 to be described below (Sec. 3.2).

3.2 LGS Wavefront Sensor

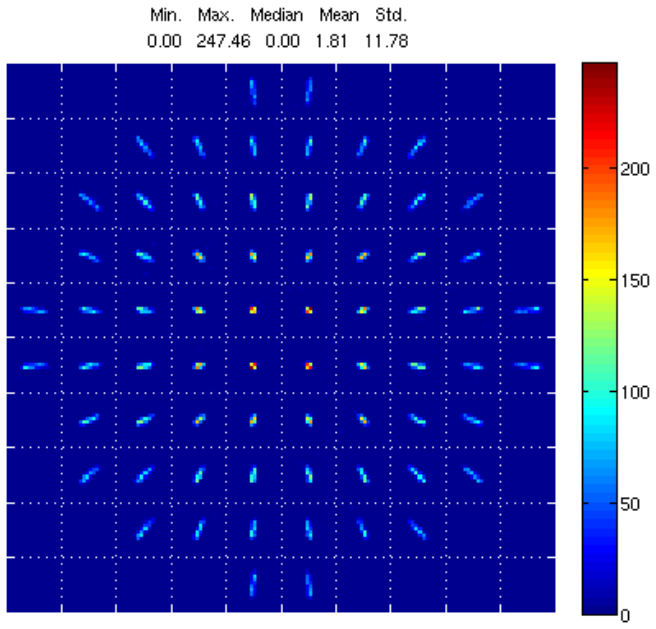

Figure 3.6: Simulated down-scaled NFIRAOS LGS WFS observation of an Na layer guide star.

The un-highlighted path in Fig. 3 shows the applications of LGS WFS measurements which are executed at the full rate of 800Hz. The Shack-Hartmann WFS (termed the LGS WFS), simulates a 10x10 WFS, corresponding to a 5m primary mirror, with 16x16 pixels per lenslet and is shown in Fig. 3.6. The scale is reduced by a factor of 6 in order to reduce computation time. The maximum elongation of the spots is held at the TMT specification of eight pixels in the subapertures on the edge of the WFS by scaling the height and thickness of the sodium layer according to the selected primary mirror diameter. It generates elongated spots based on the input phase screen and sodium profile as well as readout noise and photon noise. In the block labeled "MF Slopes" the current matched filter, R_q, is applied to the spots image $i(k)$ to obtain the estimate of the wavefront slopes,

$$\hat{\theta}(k) = R_q i(k). \tag{3.35}$$

The slopes are projected onto Zernike modes 2 through 21 at the block labeled "Slopes to Modes". The tip/tilt coefficients (modes 2 and 3) are separated from the measurement as they do not represent atmospheric tip/tilt. These modes are used as described above to estimate the matched filter gain; also, they are combined with the tip/tilt drift modes as described by Eq. 3.34 to generate the FSM tip/tilt feedback vector. This feedback vector is integrated,

$$f_{FSM}(k) = g_{FSM} e_{FSM}(k) + f_{FSM}(k-1), \tag{3.36}$$

and combined with the dither signal c_{dit} to give the FSM commands, d_{FSM}.

$$d_{FSM} = c_{dit} - f_{FSM}. \tag{3.37}$$

The remaining modes are used for the closed loop correction of the wavefront error. The modes are blended in one of two ways, (described below), with data generated by the NGS WFSs. The blended data is integrated and sent to a modal DM representation of a DM. The resulting commands form a vector representing the residual phase measured by the system.

3.3 Natural Guide Star WFSs

Two of the three NGS WFSs are implemented in the simulation: the MOR TWFS and the OI-TTF WFS. These WFSs will each use a different NGS and their integration time will be selected based on the magnitude of that star such that the proper signal to noise ratio is achieved.

3.3.1 Medium Order TWFS

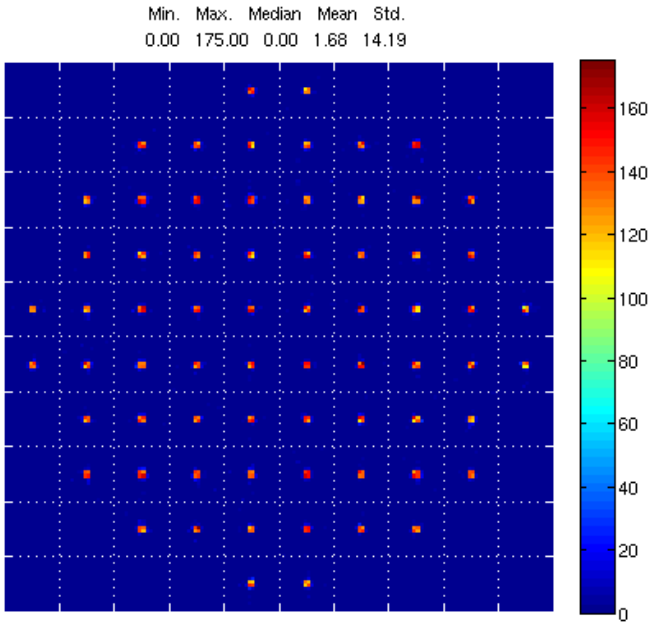

Figure 3.7: Simulated MOR-TWFS observation of unturbulated wavefronts from a NGS.

The medium order closed loop correction path is highlighted in green in Fig. 3. The MOR TWFS is also a 10x10 shack-hartmann WFS with 16x16 pixels per lenslet and is shown in Fig. 3.7. It simulates non-elongated spots from a 550nm point source along with adjustable photon noise and readout noise. The distribution of magnitudes of available guide stars for this WFS is such that the frame rate $\frac{1}{T_{MOR}}$ will fall within the range of 0.2 to 1 Hz. The rate at which the matched filter will be updated will be fixed at the selected MOR TWFS rate as it has been shown (Chapter 5) that the performance of the system is best when the two rates are equal to each other. The measured wavefront slopes are projected onto Zernike modes 5 through 21 to obtain the vector of coefficients, z_{MOR}. To simulate the slower frame rate, a boxcar average is taken which holds the output for one integration period and resets at the beginning of each period to emulate a long exposure. The output vector of Zernike coefficients

is sampled at 800Hz, scaled by a gain, g_{MOR}, and summed element-wise with the vector of medium order coefficients from the LGS WFS, z_{LGS}, to generate the MOR DM commands c_{MOR}

$$(c_{MOR})_k = (z_{LGS})_k + \frac{g_{MOR}T_s}{T_{MOR}} \sum_{j=(k-1)(T_{MOR}/T_s)+1}^{kT_{MOR}/T_s} (z_{MOR})_j. \tag{3.38}$$

3.3.2 On Instrument TTF WFS

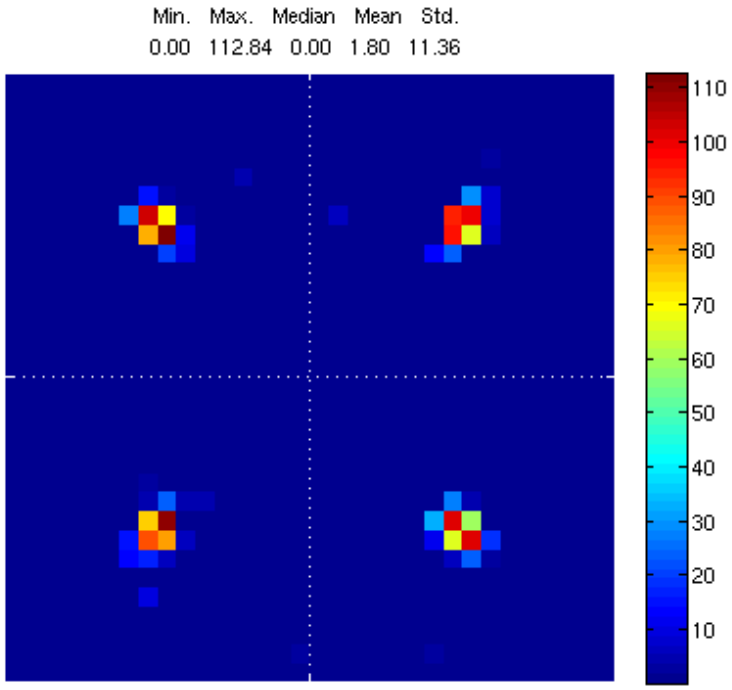

Figure 3.8: Simulated TTF WFS measurement of untrubulated wavefronts from a NGS.

The on instrument tip/tilt and focus correction path is highlighted in pink in Fig. 3. The OI-TTF WFS is a 2x2 SH-WFS with 16x16 pixels per lenslet and is shown in Fig. 3.8. It simulates non-elongated spots from a 1250nm point source

along with adjustable photon noise and readout noise. The frame rate $\frac{1}{T_{TTF}}$ of this WFS will fall in the range of 100 to 800Hz depending on the magnitude of its guide star. The measured wavefront slopes are projected onto Zernike modes 2,3 and 4 (tip, tilt and focus), the average of each coefficient is taken as in Eq. 3.38 with T_{MOR} replaced by T_{TTF}. The focus coefficient f_{TTF} is separated from the tip/tilt, the focus coefficient from the LGS WFS f_{LGS} is subtracted and the result is low pass filtered,

$$f_{LPF}(k) = \alpha_f(f_{TTF}(k) - f_{LGS}(k)) + (1 - \alpha_f)f_{LPF}(k-1), \tag{3.39}$$

and the DM focus command c_f is computed as follows:

$$c_f = f_{LPF} + f_{LGS}. \tag{3.40}$$

The tip/tilt data from the on instrument WFS is the only tip/tilt correction applied straight to the DM as there is no atmospheric turbulence information on those modes available from the LGS WFS.

3.3.3 Data Merging and Feedback

The above vectors of coefficients are concatenated to form a single vector containing DM commands for all the modes being corrected. Each coefficient is integrated and the result negated; the integrated vector is applied to a simulated modal DM which uses the Zernike coefficients to calculate the phase represented by the DM command vector. This phase is summed with the input phase screen to obtain the residual wavefront error which becomes the next input to each WFS, and thus, the loop is closed.

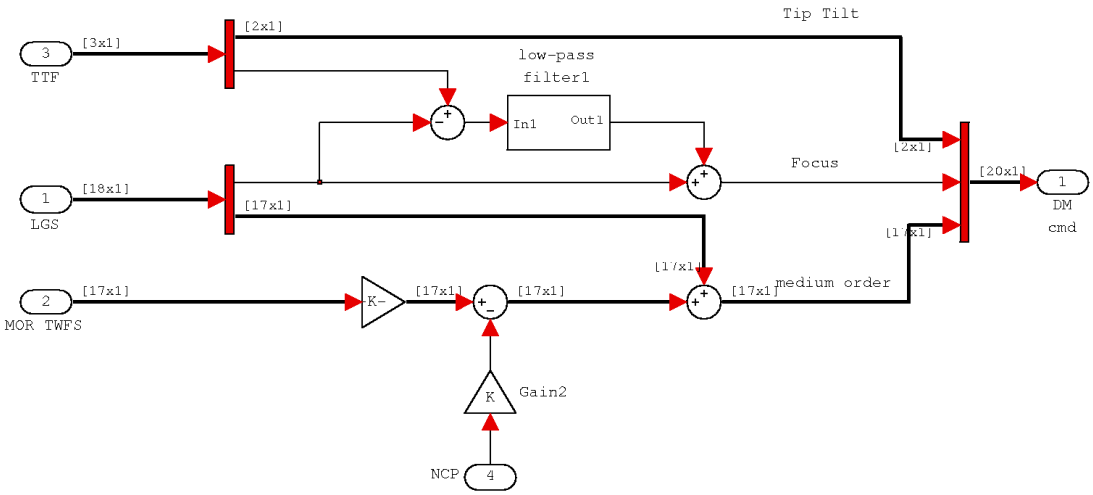

Figure 3.9: Simulink implementation of the blending of data from the three WFSs described in the previous sections.

3.4 Input Data

3.4.1 Sodium Profiles

The data set employed to generate the LGS source is sodium layer LIDAR data taken at the Large Zenith Telescope [9]. The raw data is 20ms per shot with 4.8 m altitude resolution; for the simulation input it is binned into 1 second intervals and 500m resolution. The sodium profiles are read into the simulation at 1Hz and interpolation is done between new inputs to smooth the transition.

3.4.2 Turbulence

The atmospheric turbulence is modeled using the method of Assemat et al.[19] implemented in matlab and formatted into a Simulink block. It currently generates one layer phase screens, as the simulation runs, by shifting the phase screen a fixed number of columns and generating new columns based on the existing phase screen at

each time step. The result is a non-cyclic series of turbulence which can be generated for an infinite length of time. The tip and tilt modes are removed from the LGS WFS turbulence input as this WFS is blind to those modes, see Fig. 3.10. The physical parameters used to create the phase screens are as follows:

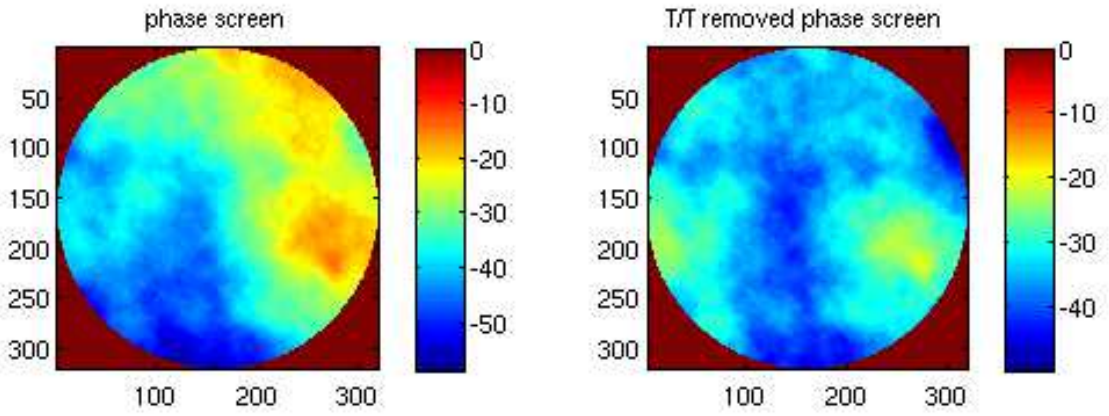

Figure 3.10: Phase screens generated by simulation for NGS WFSs (left) and tip/tilt removed for LGS WFS (right).

- Fried parameter = 0.2m,
- Outer scale = 60m,
- Wind velocity = 10m/s.

3.4.3 Initial Conditions

The gain and offset used to create a matched filter must be initialized with non-zero values. The initial conditions implemented in the simulation are generated offline; a series of 60 sodium profiles are shifted to all four dither positions and propagated through an LGS WFS object to generate a series of images of dithered elongated

spots. The initial offset is obtained by taking the mean of all the spot images. The initial gains are determined by taking the difference between the two vertical and horizontal dither positions for each profile,

$$G_x = (spots_{+vertical} - spots_{-vertical})/2 \tag{3.41}$$

$$G_y = (spots_{+horiz} - spots_{-horiz})/2. \tag{3.42}$$

The initial gains in x and y are obtained by taking the mean of G_x and G_y over all 60 sodium profiles. A poor initial condition does not appear to hinder the ability of the system to converge, nor does it appear to lengthen convergence time.

Chapter 4

Experimental Setup

Taking into account the considerations listed in Sec. 2.3, each component of the control system for NFIRAOS has been closely examined and the most effective Simulink implementation has been found in each case. The equations and subsystems presented in Chapter 3 represent a breakdown of the final design of the simulation which was then implemented on the UVic LGS test bench. The simulated hardware components described in Chapter 3 are replaced in the experimental setup by their coresponding real optical components: that is, SH-WFSs, DM, light sources, CCD cameras and optics.

4.1 Overview of UVic LGS Test Bench

The primary goal of the research undertaken on the LGS test bench is an analysis of the effects of adaptively updating the WFS centroiding algorithm as the Na layer changes. The bench utilizes experimental sodium LIDAR data taken by project collaborators.

The LGS test bench was required to reproduce the following features[20]:

- The LGS elongation along the telescope optical axis.

- The spatial and temporal variability of the Sodium atom density.
- The variability of the Sodium layer altitude.

The initial design produced a single elongated spot, representing a subaperture at the edge of a TMT LGS WFS, with dimensions of 2 by 8 pixels which corresponds to 4 arcsec of elongation on the real TMT system. The spot was generated using a 632nm laser diode as a guided point source and an extended CCD exposure. The position of the point source was moved incrementally across the camera during an exposure by applying a global tilt to a deformable mirror with each position corresponding to a 500m resolution altitude bin. The intensity of the laser diode was modulated for each position based on the sodium atom density of the corresponding altitude bin of the LIDAR data at each timestep. In addition to proving the concept, this bench also provided a preliminary demonstration of repeatability and stability for dither signal generation.

The single spot test bench demonstrated that a varying sodium profile, with the specific properties of the LGS sources to be observed by the TMT, could be produced by modulating the intensity of a laser diode while guiding it across a CCD during a single extended exposure. In order to test proposed closed loop correction control algorithms, a SH-WFS was required, and therefore, implemented by inserting a lenslet array before the CCD which emulated a scaled down version of a TMT LGS WFS. The size of the CCD camera imposed a limit of 29x29 subapertures (as opposed to NFIRAOS's 60x60) with size 16x16 pixels. In order to produce the appropriate spot elongation across all the subapertures, a defocus shape was applied to the DM in 16 steps (Fig. 4.1) leading to a symmetrical, graduated elongation which increases with distance off axis. Once again, the intensity of the laser diode was modulated according to the intensity of the altitude bin corresponding to the defocus step. A full description of this optical bench can be found in [10].

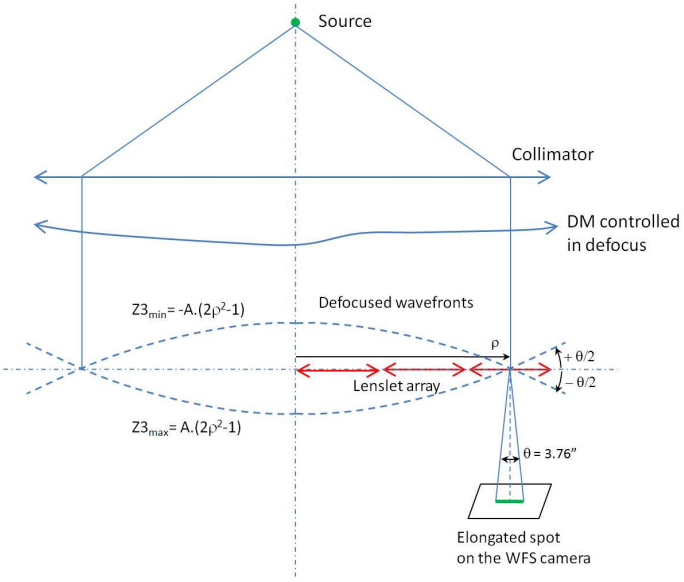

Figure 4.1: Applying a changing focus shape to the DM while modulating the source intensity yields the elongated spot pattern of the LGS WFSs of NFIRAOS.

4.1.1 The LGS/NGS Test Bench

The information used by NFIRAOS to correct aberrated wavefronts will be processed using a multi-rate control system with several different WFSs taking observations from separate sources (both natural and artificial). One of the key control issues to be tested was the blending of the data from multiple WFSs with different frame rates to command a single DM to induce the best possible correction of the atmospheric turbulence. In order to test the control scheme implemented in the Simulink model using real inputs and hardware, a more comprehensive test bench was required. The successful implementation of the single source, single WFS bench led to the design of a multi source, multi WFS test bench. In addition to the LGS, this bench also reproduces a point source NGS to be used by the MOR-TWFS and the OI-TTF WFS. In this way, the control system implemented in simulation could be tested. As outlined in [21], the requirements of the bench were to reproduce the following features in the laboratory:

- LGS–WFS with 32x32 spots, radially elongated due to the sodium layer thickness (2x8 pixels for the most elongated spots and 15x15–pixels per sub–aperture).
- Spatial and temporal variability of the sodium layer (mean altitude, thickness and vertical profile).
- Focus tracking loop, as in the NFIRAOS design, in order to follow the variation in sodium layer mean altitude.
- Dithering tip/tilt signal needed by the matched filter background algorithm.
- MOR TWFS with 12x12 non–elongated spots (FWHM=2 pixels, sub–aperture=8x8 pixels) [22].
- Complete control loop algorithm and data flow of the combined TWFSs and LGS–WFS as in the NFIRAOS RTC design and sketched in Fig. 3.
- Adjustable NGS source to control the TWFS SNR (regardless of the LGS source brightness).
- Variable frame rates for the LGS WFS (800Hz) and the MOR TWFS (0.2–5Hz) [22].
- Non–common path (NCP) aberration monitoring by an extra WFS (HASO 32x42 SH–WFS from Imagine Optic). If needed, the HASO can replace the HOL TWFS of NFIRAOS.
- Create the residual atmospheric turbulence.

As discussed in [21], Figure 4.2 presents the full optical layout of the upgraded LGS bench (created in ZEMAX). This layout features long optical paths in order to fit the available space on the optical table shared with another experiment (not

related to LGS–AO). The LGS source is a 632 nm laser diode, and the NGS source is a 785 nm laser diode. Both sources can be combined and split up with standard dichroic mirrors (hot mirrors) whose transition is located at 700nm. This choice minimizes wasted flux and pollution of sources on other cameras. A SH–WFS emulates both the fast OI-TTF WFS) and the MOR TWFS of NFIRAOS. This source, once collimated, is combined with the LGS source beam. Both beams reflect off the 22.5 mm diameter ALPAO mirror featuring 88 actuators, on a 10x10 grid. The DM action remains the same as for previous bench designs [10]. It creates LGS spot elongation with an alternating focus, the tip–tilt dithering signal required for the Matched Filter, and controllable atmospheric turbulence.

The diameter of the beam is reduced with a pair of convergent doublets (f=450 and 85 mm) to about 4 mm to match the pupil size and the spot number required for the MOR TWFS. A field lens (f=–30 mm) is introduced in a focal plane to re-image the DM pupil on the MOR TWFS lenslet array. A second hot mirror reflects the NGS beam toward the science path, and transmits the LGS beam toward the LGS WFS path. A 312.5 μm–pitch and 34 mm–focal–length lenslet array provides the 12x12 spots for the MOR TWFS. Two doublets (f=200 and 35 mm) scale the spots to match the image sampling requirements for the MOR detector (FWHM= 2 pixels). The MOR camera is a Point Grey Research Dragonfly Express IEEE1394b CCD camera featuring 480x640 7.4 μm–square pixels.

An extra pair of lenses (f=75 and 120 mm) is required on the LGS path, downstream from the hot mirror, to adjust the beam size and to re-image the pupil on the LGS WFS lenslet array. A 188 μm–pitch and 8 mm–focal–length lenslet array provides the 32x32 LGS spots. Two doublets (f=225 and 125 mm) scale the spots to match the image sampling requirements for the LGS WFS detector (FWHM= 2 pixels). The LGS WFS camera is also a Point Grey Research DragonFly Express.

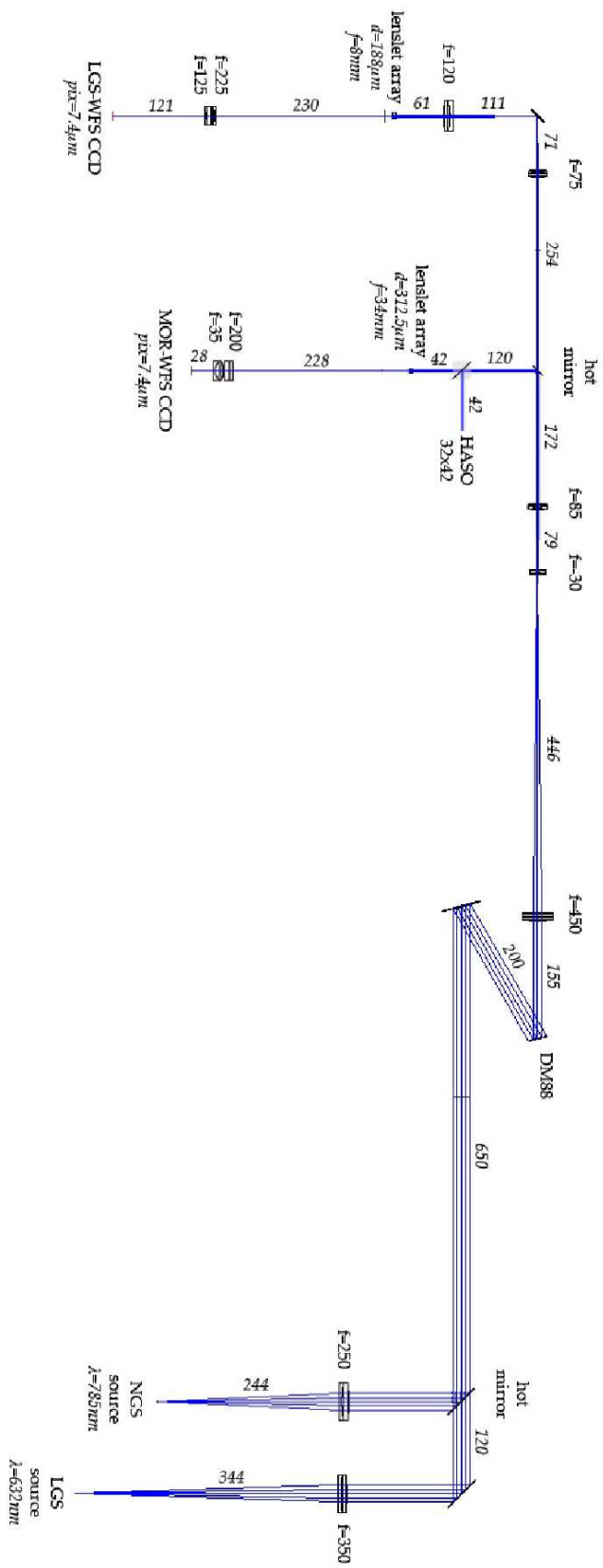

Figure 4.2: Full optical layout of the LGS bench including the MOR TWFS and the HASO WFS.

The LGS source intensity is remotely controlled and synchronized with the DM motion. The NGS source is switched on only when the DM focus is null, i.e. either at the middle of the focus ramp, or between two adjacent LGS exposures, in order to generate non–elongated spots on the NGS SH–WFS.

The frame rates planned for the NFIROAS WFSs are 800Hz for the LGS WFS, 100–800Hz for the TTF sensor, and around 0.2–5Hz for the MOR [22]. As only one camera reproduces both the TTF and MOR WFSs of NFIRAOS on the bench, it was decided to read the NGS camera at 800 Hz like the LGS camera. The NGS WFS images are time–averaged by software to generate the MOR spots at a slower frame rate. The tip–tilt and the focus modes of the TTF will be derived from the slopes measured by the NGS WFS at 800 Hz.

The bench hardware is fully controlled from a single PC (Windows OS) with Matlab/Simulink. To run faster, the drivers for the DM and the cameras are specific C–mex functions called from Matlab or Simulink. Wavefront analysis is also performed within Matlab or Simulink using the UVic AO library routines. Figure 4.3 details the hardware architecture of the LGS–bench.

A full treatment of the technical specifications and control of the test bench hardware can be found in[10], [21], [23].

4.2 Integrated Simulation and Test Bench

The simulation and test bench control software were both developed in the Simulink environment. This expedited the implementation of the simulated control system on the real system. The control scheme as described in Chapter 3 remained intact while the simulated WFSs and DMs were replaced such that the control system could create real commands to send to the DM88. Certain tasks which will be performed by the

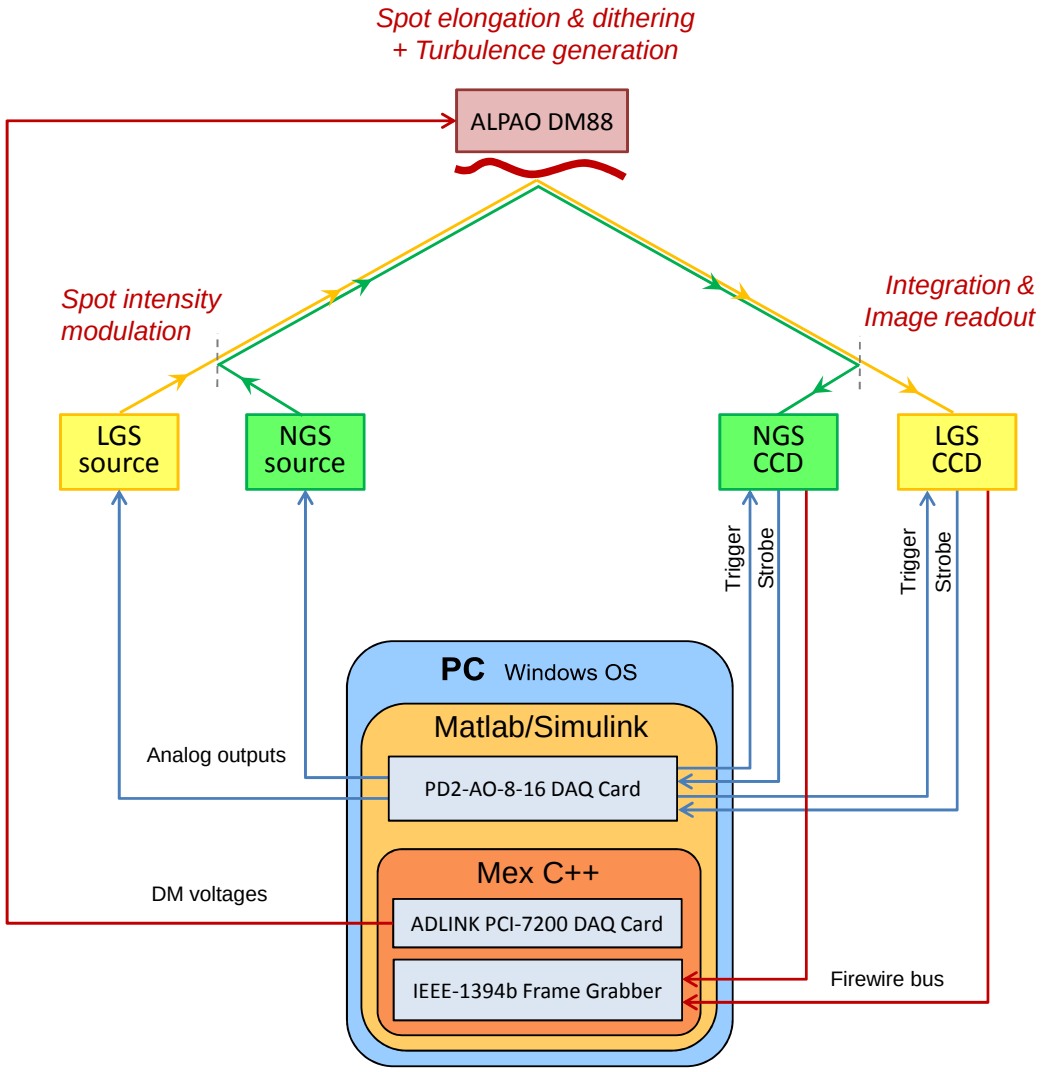

Figure 4.3: Hardware architecture of the LGS bench control system. The bench control system can be subdivided into 4 tasks: **(i) Source intensity modulation:** A 16 bit analog output PCI DAQ–card (UEI PowerDAQ PD2–AO–8–16) drives the current of both sources. **(ii) DM control:** A second PCI DAQ–card (Adlink PCI–7200) drives the DM actuators via the ALPAO electronics. **(iii) Camera control:** Both cameras must begin and end integration at varying time intervals, depending on the DM state, therefore they have been configured to be triggered externally. The UEI PowerDAQ PD2–AO–8–16 is also used for sending the trigger signals toward the cameras, which send back a strobe signal to confirm that the trigger has been successfully received. **(iv) Image acquisition:** The images of both cameras are read out via a single fast PCI frame grabber (IEEE–1394b OHCI PCI Host Adapter 3–port 800Mb/s card).

FSM in NFIRAOS (dithering and tip-tilt stabilization) are performed by the DM88 on the bench in addition to correction of atmospheric turbulence.

The most notable adjustment to the system, which was required when implementing the control system on the bench but not in simulation, was a careful calibration in order to properly merge the data from the two WFSs. Because the control is modal, the T/T, focus and the higher–order modes are extracted from the phase measured by each WFS and processed differently before being recombined to command the DM. It became apparent that a Zernike–to–voltage command matrix is required for each WFSs. Despite that modal calibration, the high–order modes were not stable in closed–loop after a few tens of seconds. On further investigation, it turned out that these long–term instabilities were not due to the controller but to small errors in the reconstructor which are accumulated over successive iterations. The DM voltages were increasing while most of the controlled Zernike coefficients remained close to zero.

To overcome this issue, it was found that the Zernike–mode–space must be common to both WFSs. The voltage–to–Zernike interaction matrix must be obtained from a modal "push–pull" sequence, and not from a zonal "push–pull" on each actuator, in order to reduce the condition number of the Zernike–to–voltage command matrix. The main steps of the calibration procedure successfully implemented and used on the bench are summarized in Appendix A.

Chapter 5

Simulated and Experimental Results

5.1 Simulation Results

The major objective of constructing the Simulink model was to implement and adapt the proposed control architecture such that it produced stable correction, free of corruption from sodium layer changes, in closed loop over long time periods. The top level of the final Simulink model is shown in Fig. 5.1, the components and subsystems of the successfully implemented simulation are described in Chapter 3 and the results will be discussed below.

5.1.1 Stable Closed Loop Correction

A demonstration of long term stability of the closed loop system was the first critical target. Fine tuning and exploration of the parameter space could only be carried out once all components were successfully integrated. The top panel of Fig. 5.2 shows a time series of the rms of the residual phase; that is, the rms of the aberrations

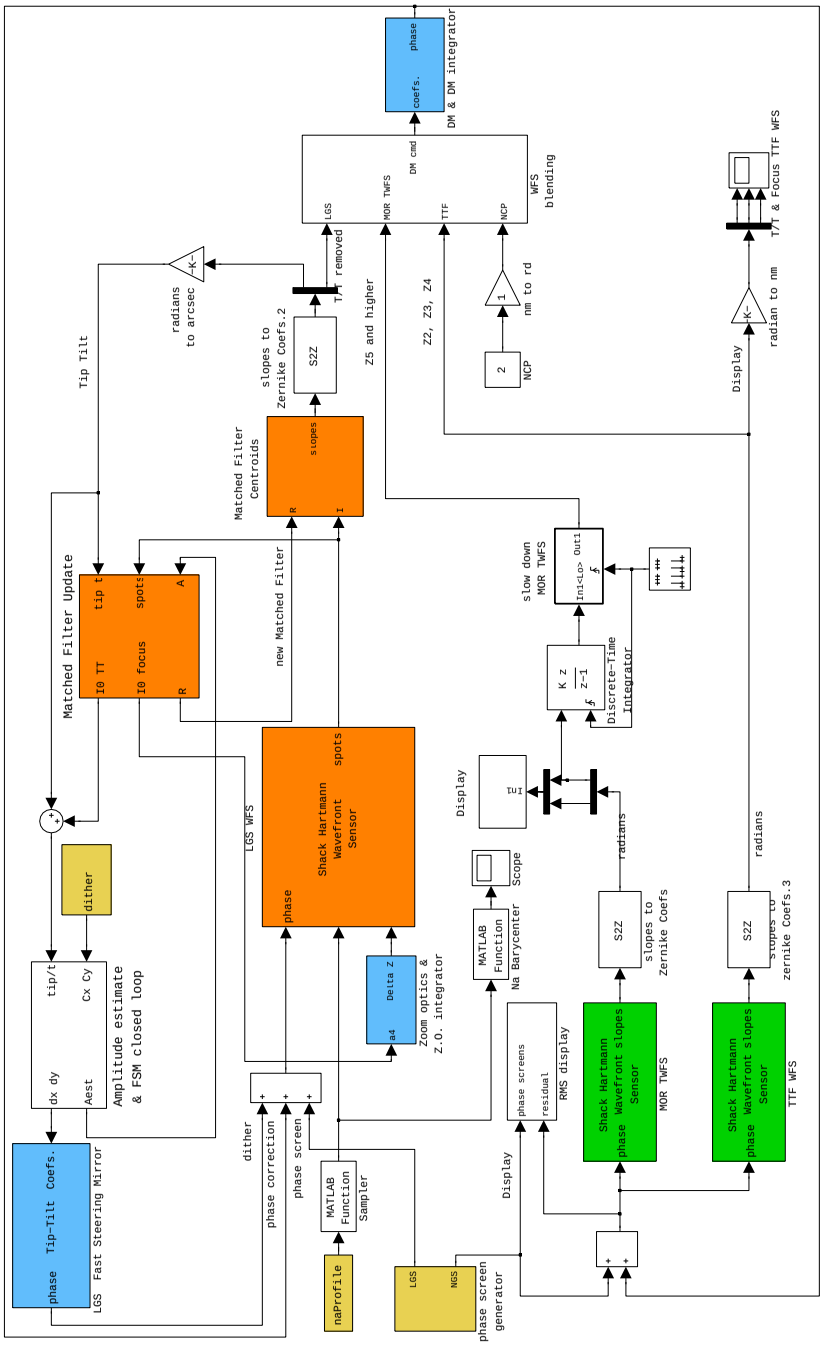

Figure 5.1: Simulink model of NFIRAOS control system.

remaining in the wavefront after striking the DM while closed loop correction is being applied. This corrected wavefront would, at the point measured, be diverted to a science camera and thus indicates the quality of correction. The simulated time period is 60 seconds (simulation time) with the full speed operations occurring at 800Hz and the background tasks occurring at 0.3Hz, thus showing significant and stable correction over many iterations of all closed loops. In addition to long term stability, the NFIRAOS design requires that the system converge in less than 20s once closed loop correction is initiated. This constraint is due to the great expense associated with each minute of observing time on the TMT; dead time in which useful observation data cannot be acquired must be minimized. The bottom panel of Fig. 5.2 shows the first $1/10^{th}$ second of the simulation; it can be seen that the 20 second criterion was easily met without requiring any modifications to the system, even with background tasks executed at the slow end of their range. No stable case was encountered in which this criterion was not met.

Typically, the rms of the phase screens used to simulate turbulence fell in the range of 400-2500nm and the resulting residual phase rms was measured in the range of approximately 50-300nm. As the long term performance of the system was of significant interest in this study, a time average of the rms of both input and residual phase was maintained. The top two panels of Fig. 5.3 show a typical result wherein the average over time of the input rms converged to approximately 800nm and the residual converged to 100nm rms for a 60 second simulation. The bottom panel of Fig. 5.3 is the ratio of residual to input which shows the percentage of input phase which is not corrected. It indicates that, on average, 86.5% of the input phase is corrected by the system. The phase screens were generated using a set of given parameters which are held constant for all simulations but are seeded by a random number to create the first of the series; some variation between simulations is therefore expected.

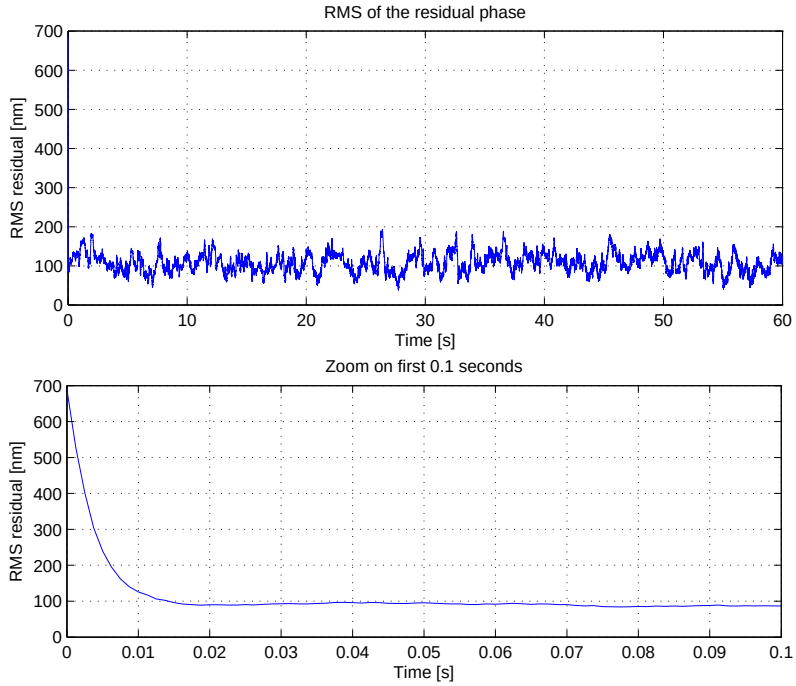

Figure 5.2: Top: rms of the residual phase measured at the point where the science path would be. Bottom: zoom on first 0.1 second of the simulation.

A good visual representation of the closed loop correction can be seen by observing the spots change on the WFSs. The effect is most easily seen on the OI-TTF WFS; Fig 5.4 shows three frames from a closed loop simulation. They are the first, fourth and seventh frames taken at a rate of 800 Hz. Therefore, good visual correction is achieved quickly after the loop is closed.

5.1.2 Effects of a Dynamic Sodium Layer

The motivation for using the matched filter algorithm was to minimize errors due tospot elongation and sodium layer induced LGS aberrations. To verify that this was achieved, it was necessary to decouple contributions to the residual phase which were the result of turbulence from those resulting from sodium layer fluctuations. The simulation was run for 60s with a static sodium profile and then repeated for 60s with a dynamic sodium profile; the rms of the time series of residual coefficients of

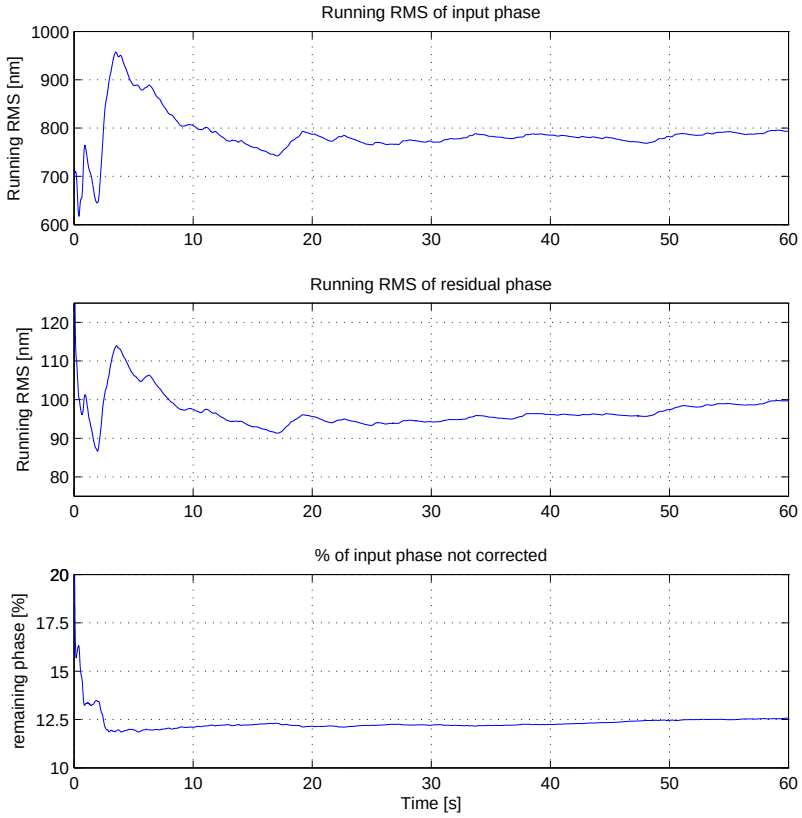

Figure 5.3: Top: time averaged rms of the input phase screens. Middle: time averaged rms of the residual phase. Bottom: % of input phase remaining in wavefront.

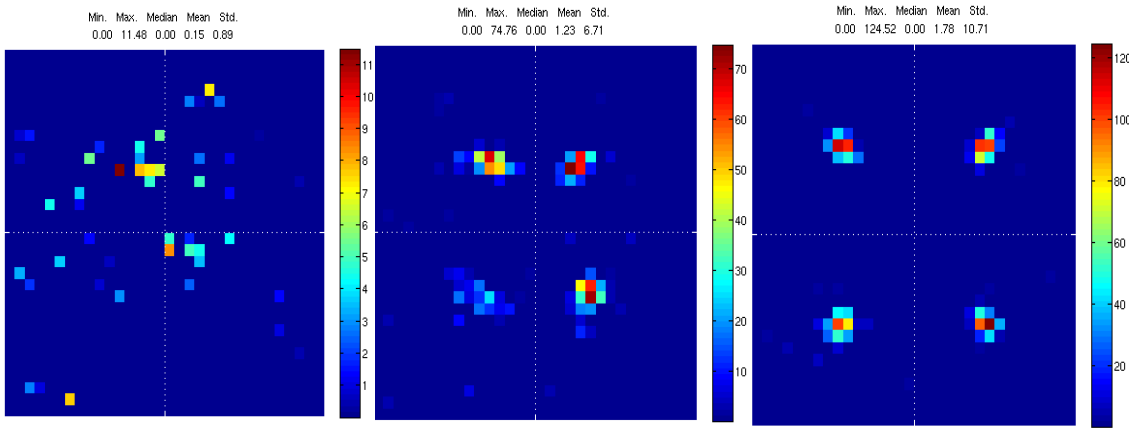

Figure 5.4: Spots on the OI-TTF WFS converge as the closed loop correction proceeds.

Zernike modes 2-21 were compared with the expectation that a minimal reduction in performance would occur. Fig. 5.5 shows that the case in which a dynamic sodium profile was used yielded only a small increase in the rms of some of the modes. The first three modes (z = 2,3,4) corresponding to tip, tilt and focus, are effectively equal for both cases; this was expected as the OI-TTF WFS provides fast correction from an NGS and does not suffer from any sodium layer effects. For a baseline comparison, see Fig. 5.11 which demonstrates the performance of a uniform threshold Centre of Gravity centroiding algorithm compared to a matched filter when measuring the LGS aberrations induced by a dynamic sodium profile. The sodium profile data used in all cases was extracted from the LZT LIDAR data displayed in Fig 1.5.

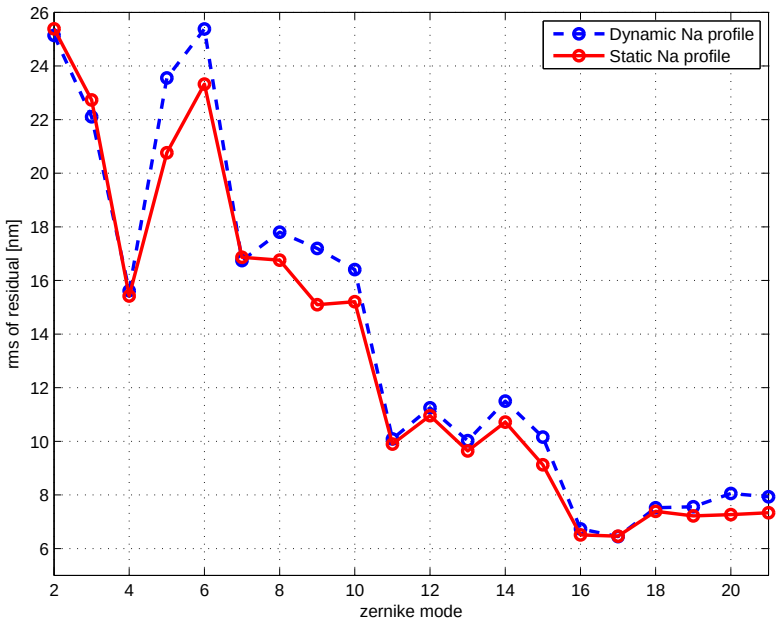

Figure 5.5: Difference in residual rms of the coefficients of Zernike modes 2-21 when sodium profile is static and dynamic.

5.1.3 Comparison with an Analytical Model

A transfer function based analytical model was developed in order to gain a more complete understanding of the way in which the different closed loops interact with each other at different rates as well as to determine a rough estimate of the stable range for certain gain parameters. The theory and construction of the model is presented in Appendix B. The MOR-TWFS acts as a low-pass filter (LPF) due to its slower frame rate, and the matched filter is by nature a high-pass filter (HPF) as the periodic updates render it blind to low frequencies. By making the HPF and LPF complementary, such that *HPF = 1-LPF*, both WFSs work in tandem without any conflict, they are equivalent to a single WFS sensing all the temporal frequencies. In order to achieve this complementarity, the background tasks of updating the matched filter and applying a MOR TWFS correction to the DM must be executed at the same rate. In this case, the Bode plot of the system indicated that it should behave as a single integrator. The coefficients of Zernike modes greater than 4 from each WFS are combined with a straight sum with a gain g_{MOR} applied to the slower MOR-TWFS data, as defined in Eq.3.38. When the two WFS are complementary, the OL transfer function of the system indicates that stability should be maintained for $0 < g_{MOR} < 5$. When the two update rates differ by some ratio, the range of stability for g_{MOR} is reduced; the absolute rate of each loop is irrelevant. Only the relation between the rates affects the stable parameter range.

To verify the accuracy of the predictions made by the analytical model described in Appendix B, two conditions were selected to compare simulation and predicted results. In the first case, the matched filter was updated five times faster than the MOR TWFS. This situation could occur if the guide star being used by the MOR TWFS had a high magnitude which would require a longer integration to achieve the minimum SNR. The prediction, based on the gain and phase margins, made by

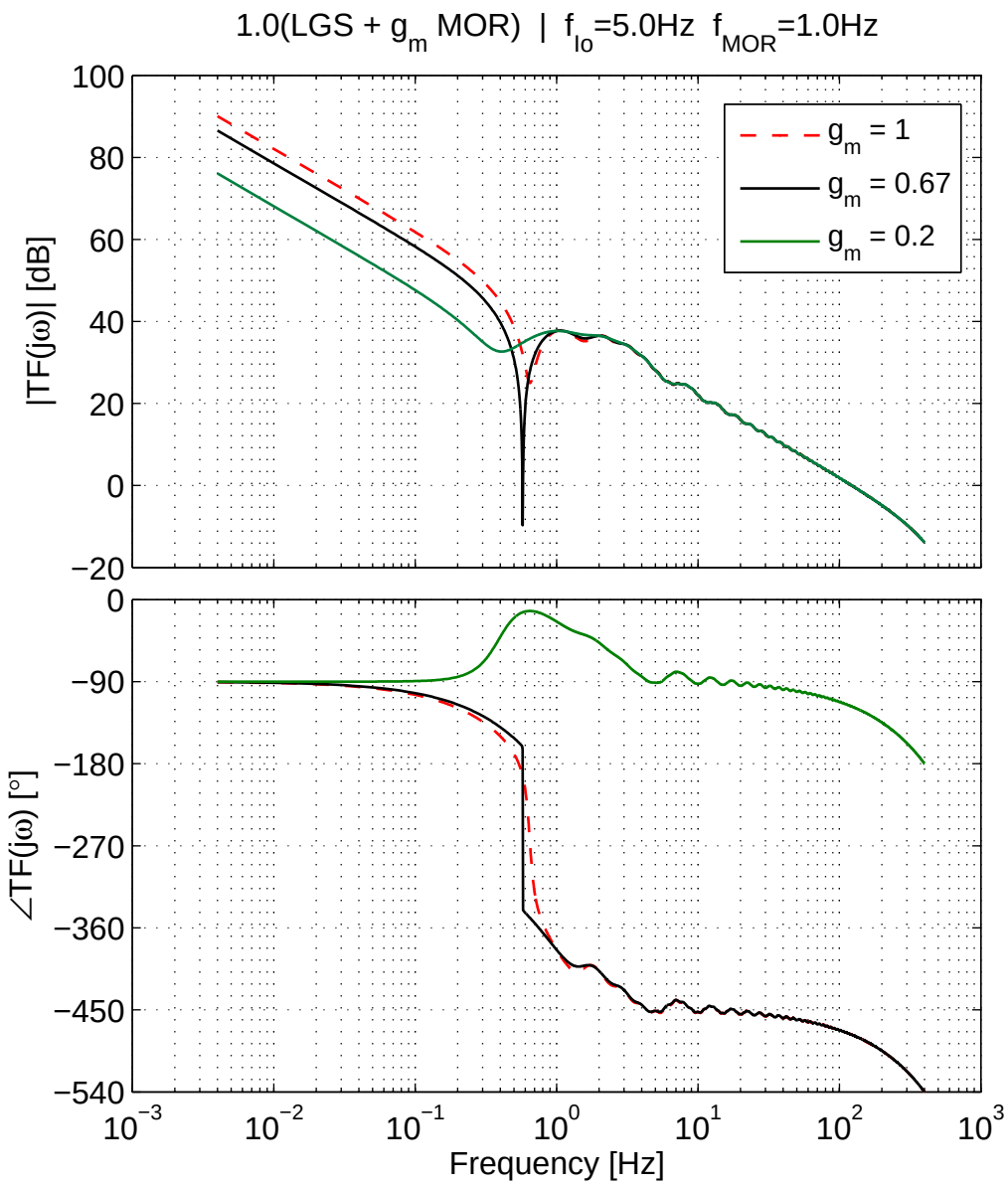

Figure 5.6: For a fixed DM integrator gain and a 5:1 ratio between matched filter updates and MOR TWFS frame rate, the resulting theoretical bode plot is shown for three different values of g_{MOR}.

the analytical model when the ratio of the rates is 5:1, shows that for any given gain on the DM integrator (0-1) applied to the final feedback command, the system should be stable when $0 < g_{MOR} < 0.67$. Fig. 5.6 is generated from the theoretical transfer function and shows the differences in the Bode plot of the system as g_{MOR} is increased. As g_{MOR} reaches 0.67, there is an abrupt change in the shape of the Bode plot. The gain margin becomes negative and thus the system becomes unstable.

Using this prediction as a starting point, the simulation was run for various DM gains and a g_{MOR} of either 0.6 or 0.7. It was found that, except for a DM gain approaching one, the simulation was stable when g_{MOR} had a value of 0.6 and unstable at a value of 0.7 (Fig. 5.7). The increasing oscillations observed in simulation for higher closed loop gains is likely due to the reduced gain and phase margins when that parameter is high. While still theoretically stable, the system is more easily perturbed.

In the second case, both the matched filter update and the MOR TWFS integration time were set to 0.3Hz which falls within the range stated in Sec. 3.3.1 for probable MOR TWFS rates. The prediction made by the analytical model when the two rates are equal show that for $0 < g_{MOR} < 5$ the system should be stable, i.e. positive phase and gain margins for g_{MOR} in that range. However, in simulation when equal rates are used, the system exhibits increasingly oscillatory behaviour and ultimately instability for g_{MOR} approaching one. While this indicates that the analytical model does not exactly match the transfer function of the simulation, the analysis gave a good indication that the greatest stable parameter range becomes available when both background rates are equal. It showed that when the rates are not equal, there is a dominant change in the system transfer function which causes an experimentally verified reduction in the range of certain parameters. It would be possible to characterize these stable ranges for various ratios of the two background

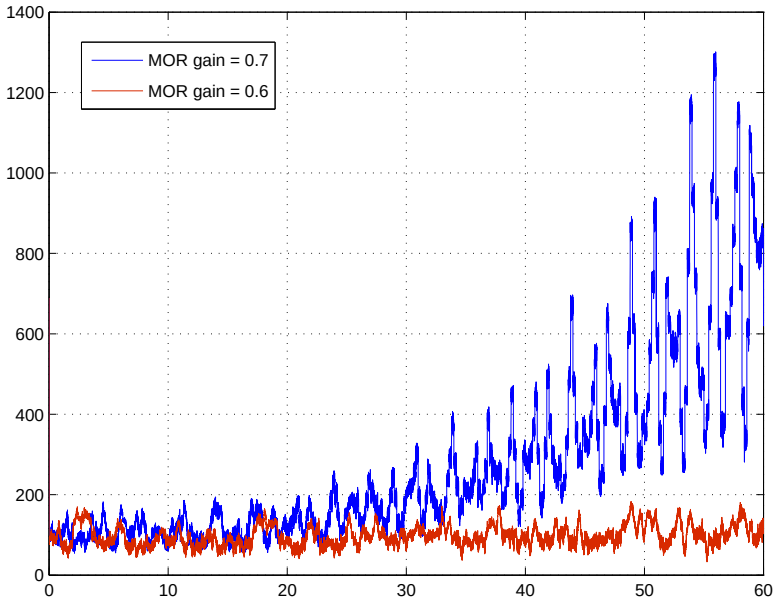

Figure 5.7: The rms of the residual phase from simulations run with a 5:1 ratio between matched filter update rate and MOR TWFS frame rate when $g_{MOR} = 0.6$ and $g_{MOR} = 0.7$.

rates examined using the analytical model as a starting point. This would be done in the event that it was decided to fix the matched filter update rate independently of the MOR TWFS rate. This was considered a beneficial option, as the matched filter update rate will affect the rejection of the LGS disturbances, whereas the MOR TWFS rate will affect the rejection of low (temporal) frequency turbulence. The two rejections are linked, however, due to the LP-HP filter relation between the matched filter update and the MOR TWFS frame rate. The plot of Fig. 5.8 shows that if the matched filter update rate is faster than the MOR TWFS frame rate, the rejection of the turbulence is worse for the low frequencies and the system can be unstable. If the matched filter update is slower than the MOR frame rate, the rejection of the slowest turbulence is better, but the rejection of the slow LGS disturbances is worse.

In light of this analysis, it has been decided, as indicated in Sec. 3.3.1, that a valid

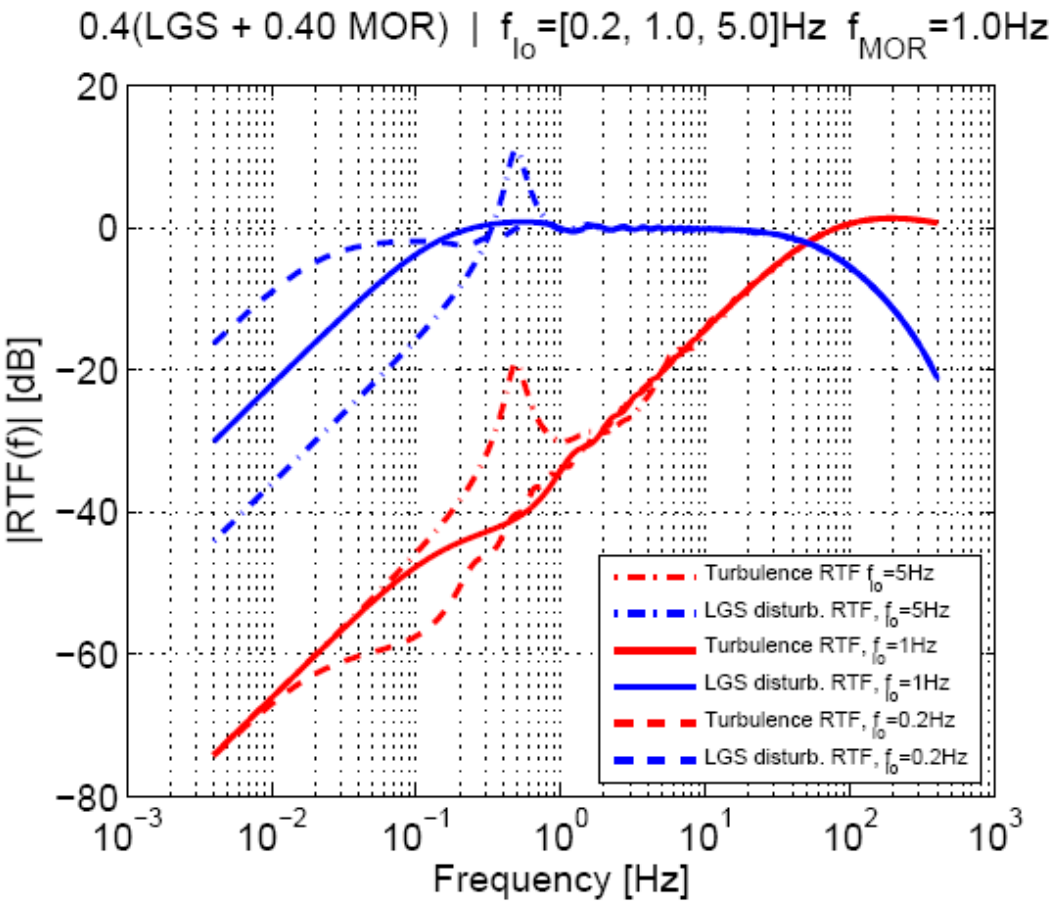

Figure 5.8: Turbulence and Sodium layer disturbance Rejection Transfer Functions for different update rates f_{Io} of the Matched Filter reference image. Integrator gain g is 0.4, the MOR gain is 0.4 also.

method of selecting the rates of the background tasks for any given set of observation conditions will be to set the frame rate of the MOR TWFS based on the magnitude of its NGS and use the same rate to update the matched filter. Estimates of the required update rate of the matched filter when applied to correction of Na layer disturbances were placed at 0.1 - 10Hz[13]. Since this includes the more well defined range of frame rates of 0.2-5Hz for the MOR TWFS, it has been deemed an acceptable method of selecting the background rate.

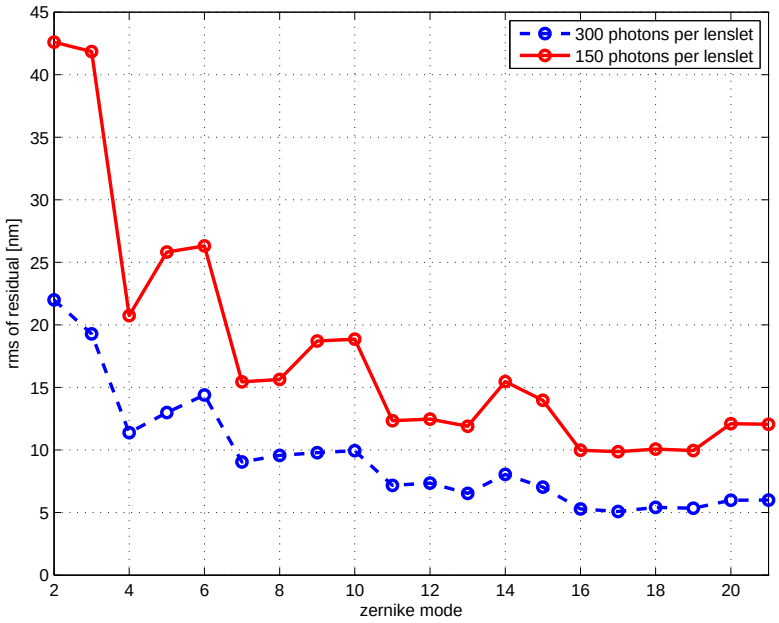

Figure 5.9: The reduction in performance of the system when a higher magnitude NGS is used for the MOR TWFS.

5.1.4 Magnitude of MOR TWFS NGS Reference

The TWFSs will use reference stars available within the field of view. The distribution of appropriate NGS candidates available at any given time of night or year spans several magnitudes and the photon flux incident upon the WFSs will not be constant for observations made using different guide stars. The MOR TWFS will be constrained to maintain a minimum SNR, and thus the integration time must be increased for higher magnitude NGSs (corresponding to lower flux). The effects on the residual phase due to a reduced photon flux incident on the MOR TWFS in the simulation were examined by reducing the number of photons per pixel available to the WFS. It was predicted that an increase in residual phase would occur due to the reduction in photon flux. This is confirmed in Fig. 5.9.

It was also found that a significant portion of the performance quality could be regained by lengthening the exposure time of the MOR TWFS. In light of the results

obtained in Sec 5.1.3, the matched filter update rate was also required to be reduced as the integration time of the MOR TWFS was lengthened.

5.2 Experimental LGS Test Bench Results

The UVic LGS test bench, described in Chapter 4, successfully reproduced both the elongated spots on the LGS WFS and the non-elongated spots on the NGS TWFS (Fig. 5.10).

The control system simulator was ported to the UVic LGS bench and several tests were run to ensure that the control system met the goals outlined for the simulation. First, after development of the DM calibration procedure described in Appendix A, long term stability was achieved; stable correction over 200s of running time was successfully demonstrated along with convergence in less than 20s. As a baseline for performance comparison, the zernike decomposition (modes 2-40) of open loop LGS WFS phase measurements of a turbulence-free time series of images generated from a dynamic set of sodium profiles was obtained for two cases: measurements were made by a matched filter, and, simultaneously, by a uniform threshold centre of gravity (CoG) algorithm. The resulting aberrations measured by each algorithm are shown in Fig. 5.11. The most prominent aberrations induced on measurements of radially elongated LGSs spots due to the Na layer fluctuations are centro-symmetric modes such as focus (Z_4) and spherical aberrations (Z_{11}, Z_{22}, etc), and square-symmetric modes such as tetrafoils (Z_{14}, Z_{26}, etc). The focus error is a real optical aberration and is corrected by the zoom optics (Sec. 3.1.4). Aberrations in the absence of atmospheric turbulence beyond focus, are mainly artefacts of the LGS wavefront sensing of elongated spots. According to previous investigations [10],[24], the spherical aberrations are due to a truncation of asymmetric LGS spots by a circular field-stop.

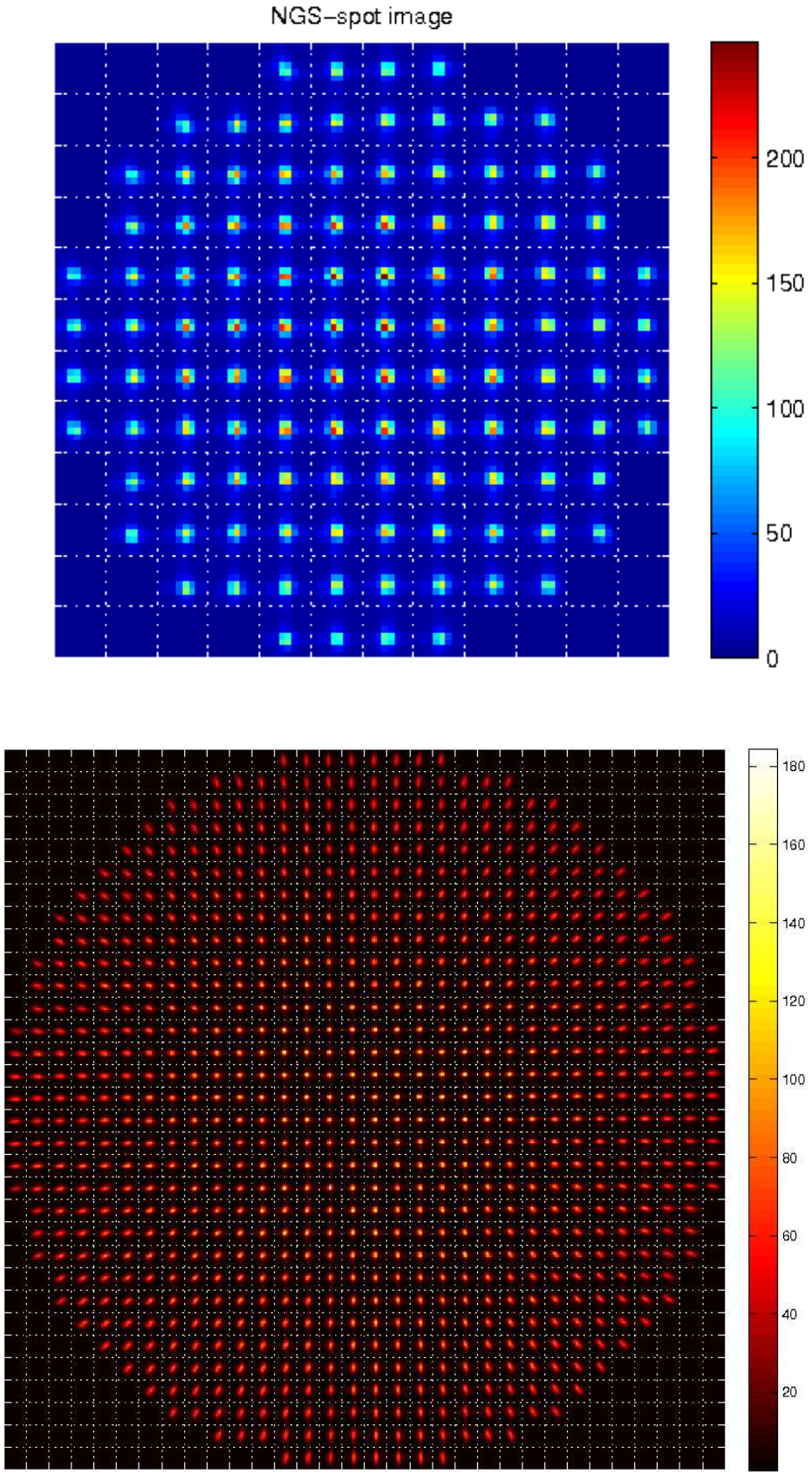

Figure 5.10: NGS TWFS spots (top) and elongated LGS WFS spots (bottom) generated by LGS test bench.

Fig. 5.11 shows that Z_{11} is significantly reduced when a matched filter is used. Square-symmetric modes are likely due to spot truncation by square pixel boundaries, spot overlap and sampling effects on centroid measurements. The use of a polar coordinate CCD array will mitigate these aberrations[25].

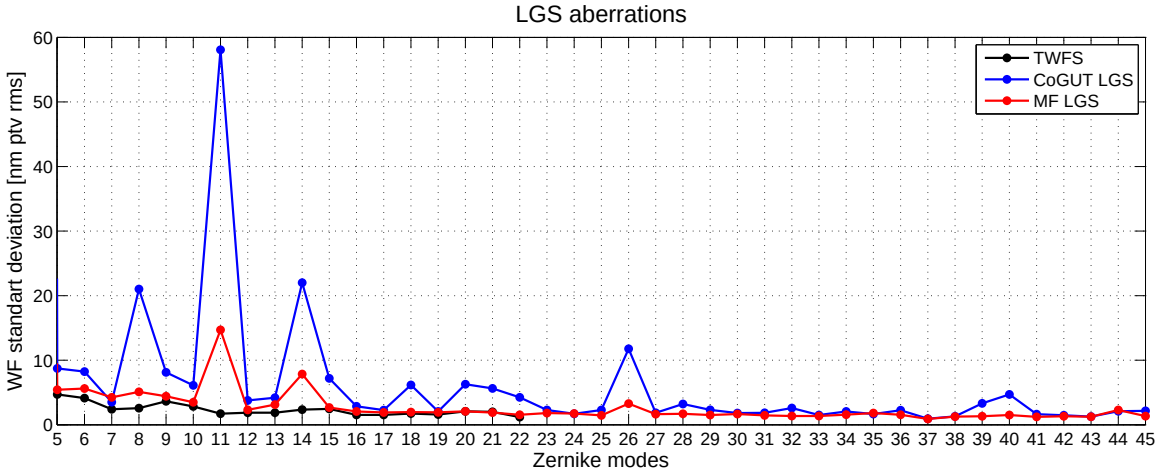

Figure 5.11: Comparison between matched filter and CoG measurements of LGS disturbances.

Chapter 6

Conclusions

In Chapter 1, it was shown that the Thirty Meter Telescope will need to employ a LGS-AO system due to the restricted sky-coverage provided by NGS AO systems. The various issues for existing AO systems which can hamper wavefront correction arising from the use of an artificial guide source were then posed and their solutions presented. The additional difficulties faced by the TMT are the result of a combination of the large size of its primary mirror and the properties of the atmospheric sodium (Na) layer. The Na layer is located at a mean altitude of 90km and its mean thickness is 10km. Viewing the column of excited Na atoms from 15m off-axis (as will be the case for the TMT) will lead to nearly 4 arcseconds of elongation. On the TMT this will correspond to WFS spots which vary from 2x2 pixels to 2x8 pixels as distance off axis is increased from 0m to 15m.

The TMT's first light AO facility, NFIRAOS, will be a system that provides near diffraction-limited correction of aberrated wavefronts. It will be a LGS-AO system on an ELT and will thus be designed to overcome the many challenges associated with such a system. It will mitigate the cone effect by using multiple LGSs, measure atmospheric tip/tilt by using a NGS and prevent degredation of the science image

due to Na layer fluctuations and measurement artefacts of elongated WFS spots by employing a temporal filtering approach where-by the LGS system will be blind to low temporal frequency changes. The slowly changing atmospheric turbulence which will be missed by the LGS WFSs will be sensed by NGS WFSs in order to provide correction over the entire temporal spectrum.

The simulated control system was presented as a block diagram at the beginning of Chapter 3. This is the control process which is now proposed for the LGS wavefront sensing on NFIRAOS in order to provide the required quality of correction by mitigating the issues presented in the first two chapters. The original control model has been modified such that the system is stable over long time periods of closed loop correction. The remainder of Chapter 3 provides the details of each processing step that occurs in the simulation and their implementation in Simulink is shown. It elaborates on the construction of the constrained Matched Filter and shows the way in which the data from multiple WFSs collecting data at different frame rates is merged to form a command for a single DM.

Concurrent to the development of the NFIRAOS control system simulation, an optical test bench was developed that emulates the NFIRAOS environment. In its final form, it reproduced the elongated LGS WFS spots and the non-elongated NGS WFS spots using two separate laser diode sources. Chapter 4 gave the details of the optical layout and hardware of the LGS test bench. Once bench and simulation were complete, the control system model was implemented on the real system by replacing the simulated hardware and input signals with the real light sources and data taken by the WFSs on the bench. Some modifications to the Matlab code were required and it was found that, for a real system, careful DM calibration is required in order to maintain longterm stability; therefore, some extra steps had to be introduced to the data merging block.

The fully developed simulation described in Chapter 3 was tested for several key performance requirements and the results of these tests were described in Chapter 5. Results showed that the system was stable over long term closed loop correction runs when using all three WFSs. Dynamic Na layer data was used and atmospheric turbulence, readout noise and photon noise were present. Under these conditions the system converged in under 20s in all stable cases. This is a telescope operational requirement due to the high cost of each minute of observing time; time spent waiting for the AO system to converge will be expensive and it must be minimized. A comparison between correction quality when the Na layer was static and when it was dynamic was made in order to ascertain that the matched filter was effectively rejecting the Na layer fluctuations. A minimal reduction in correction quality was experienced by the system when the Na layer is dynamic. For a comparison to conventional centroiding techniques, the performance of the matched filter and that of a uniformly thresholded centre of gravity algorithm was observed using the LGS test bench once it was integrated with the control system. This showed that the matched filter measured significantly less of the Na layer induced aberrations than the CoG.

The control system has a large parameter space which is difficult to optimize with a computationally expensive simulation. For this reason, an analytical model of the control system was developed and the transfer functions used to predict stable ranges for various parameters. It was also useful for developing an understanding of the interactions between the various closed loops in a multirate system. It was found that the ratio of the update rate of the matched filter to the frame rate of the MOR TWFS had the largest impact on the shape the bode diagram of the system and that the system behaviour approaches that of a single integrator when these two rates are equal. When this is the case the two WFSs are complementary HP-LP filters to the atmospheric turbulence and correction of the entire temporal spectrum without gaps

or overlaps is possible. As a result of this analysis, it was decided to fix the matched filter update rate at the frame rate of the MOR TWFS. It was also shown that the magnitude of the guide star used by the MOR TWFS can affect the performance of the system, and that for a higher magnitude NGS, it is necessary to increase the integration time of the MOR TWFS in order to maintain a minimum SNR on that instrument. It was found that this will recover most of the correction but the system response will not be identical because the corner frequency of the HP-LP filters has been shifted to allow for the longer integration time.

A simulation of the control system of the LGS wavefront sensing for NFIRAOS was successfully implemented in the Matlab Simulink environment. It was shown to meet the stated stability, convergence and correction quality requirements. Once developed in simulation, the control system was implemented on the UVic LGS test bench and the performance also met the above requirements.

Future work which will build on this project should include:

- Expansion of the simulation to a multiconjugate system (addition of a second DM)
- Concurrent enhancement of the UVic LGS test bench to reflect changes in the simulation.
- Further development of the UVic LGS test bench to reproduce multiple LGS sources over the field of view in order to investigate tomography.
- A comparitive study of the performance of centroiding algorithms other than the matched filter.

Continuing work in this area will provide improved understanding and expand knowledge regarding the behaviour of AO systems for ELTs, and will thus enable their designs to be improved.

Bibliography

[1] European Southern Observatory, "The european extremely large telescope." `www.eso.org/public/astronomy/teles-instr/e-elt.html`, 2009.

[2] Giant Magellan Telescope Organization, "Giant magellan telescope." `www.gmto.org`, 2009.

[3] TMT collaborators, "Thirty meter telescope." `www.tmt.org`, 2009.

[4] NRC-NSERC Long Range Planning Panel, "The origins of structure in the universe: Canadian astronomy and astrophysics in the 21st century.," tech. rep., CASCA, 2000.

[5] J. C. Wyngaard, "Atmospheric turbulence," *Annu. Rev. Fluid Mech.*, vol. 24, 1992.

[6] R. Clare and E. Ellerbroek, "Adaptive optics sky coverage estimates for the TMT," TMT.AOS.TEC.05.029.DRF04, 2005.

[7] NRC-HIA Astronomy Technology Research Group et. al., "NFIRAOS RTC algorithm description," TMT.AO.DRD.08.002.REL04, 2008.

[8] R. Dekany, "Guidelines for adaptive optics risk assessment," TMT.AOS.COR.04.099.DRF01, 2004.

[9] T. Pfrommer, P. Hickson, and C.-Y. She, "A large-aperture sodium fluorescence lidar with very high resolution for mesopause dynamics and adaptive optics studies," *Geophys. Res. Lett.*, vol. 36, 2009.

[10] O. Lardiere, R. Conan, C. Bradley, K. Jackson, and G. Herriot, "A laser guide star wavefront sensor bench demonstrator for TMT," *Optics Express*, vol. 16, no. 8, 2008.

[11] G. Herriot, P. Hickson, and B. Ellerbroek et. al., "NFIRAOS: TMT narrow field near-infrared facility adaptive optics," in *Adavances in Adaptive Optics II*, vol. 6272, Proc. SPIE, June 2006.

[12] NRC-HIA Astronomy Technology Research Group, "Conceptual design of NFIRAOS," TMT.AOS.CDD.06.010.REL02, 2006.

[13] NRC-HIA Astronomy Technology Research Group et. al., "Preliminary design report nfiraos," TMT.AOS.PDD.08.020.REL01, 2008.

[14] L. Gilles and B. Ellerbroek, "Shack-hartmann wavefront sensing with elongated sodium laser beacons: controiding versus matched filtering.," *Applied Optics*, vol. 45, no. 25, 2006.

[15] L. Gilles and B. L. Ellerbroek, "Constrained matched filtering for extended dynamic range and improved noise rejection for shack-hartmann wavefront sensing," *Opt Lett.*, vol. 33, 2008.

[16] S. Druel, "Algorithm development for TMT NFIRAOS offset and gain estimation of LGS WFS," TMT.AOS.TEC.07.026.DRF01, 2007.

[17] K. Jackson, "Laser guide star wavefront sensor sodium variability tracking simulation." Undergraduate honours thesis, UBC Dept. of Physics and Astronomy, 2008.

[18] R. Conan. `web.uvic.ca/~rconan/pub/aoLibDoc/`, 2009.

[19] F. Assemat, R. Wilson, and E. Gendron, "Method for simulating infintely long and non stationary phase screens with optimized memory storage," *Optics Express*, vol. 14, no. 3, 2006.

[20] R. Conan and C. Bradley, "Performance assessment of laser guide star wavefront sensing." TMT Work Package TMT.AOS.CON.06.038.REL01, 2008.

[21] R. Conan, O. Lardiere, and K. Jackson, "Uvic ao lab laser guide star test bed upgrade: Final report," TMT.SEN.CON.09.001.CCR01, 2009.

[22] D. Andersen, R. Conan, B. Ellerbroek, G. Herriot, and J.-P. Veran, "Negating effects from sodium profile variations for TMT: The mor truth wavefront sensor of NFIRAOS," in *Adavanced Wavefront Control: Methods, Devices and Applications VI*, vol. 7093, Proc. SPIE Optics + Photonics 2008, August 2008.

[23] O. Lardiere, R. Conan, C. Bradley, G. Herriot, and K. Jackson, "Laser–guide–star wavefront sensing for TMT: Experimental results of the Matched Fitering," in *Adaptive Optics Systems*, Proc. SPIE Astronomical Telescopes and Instrumentation, 2008. (accepted).

[24] R. M. Clare, M. A. van Dam, and A. H. Bouches, "Modeling low order aberrations in laser guide star adaptive optics systems," *Opt. Express*, vol. 15, 2007.

[25] S. Adkins, "A polar coordinate CCD array for LGS AO," TMT.AOS.COR.06.008.DRF01, 2006.

Appendix A

Modal calibration for test bench

The main steps of the calibration procedure successfully implemented and used on the bench are summarized here:

1. Computation of the voltages–to–slopes interaction matrix of the LGS WFS with a zonal "push–pull" sequence.

2. Calibration in closed–loop, with the LGS WFS, of the voltages generating each Zernike mode (Z_2 to Z_{45}). The voltages obtained are stored as a matrix V_Z.

3. Computation of the voltages–to–Zernike interaction matrix D_{LGS} and D_{NGS} for both WFSs respectively, with a modal "push–pull" using the columns of V_Z as input for the DM voltages.

If u is the voltage vector projected on the voltage basis V_Z, then the Zernike coefficients measured by the LGS and the NGS WFSs are respectively:

$$\begin{cases} z_{LGS} = D_{LGS}\, u \\ z_{NGS} = D_{NGS}\, u \end{cases} \tag{A.1}$$

Hence, the Zernike coefficients z_{NGS} seen by the NGS WFS can be converted in term of LGS-like Zernike coefficients z'_{LGS}, as if they would be seen by the LGS WFS:

$$z'_{LGS} = D^{+}_{NGS}\, D_{LGS}\, z_{NGS}. \tag{A.2}$$

The operator $^{+}$ denotes the pseudo–inverse of the matrices. The product $D^{+}_{NGS}\, D_{LGS}$ could be termed a "Zernike–to–Zernike" command matrix, as it transforms NGS Zernike to LGS–like Zernike coefficients. As the length of the vector z_{NGS} is lower than those of z_{LGS}, some zeros must be added to fill the modes beyond Z_{22}.

Thanks to this transformation, the Zernike coefficients coming from the NGS WFS can be added to those coming from the LGS WFS, and converted into a voltage command for the DM using the calibrated voltages V_Z, as follow:

$$v_{DM} = V_Z\, D^{+}_{LGS}\, (z_{LGS} + g_m z'_{LGS}) \tag{A.3}$$

Appendix B

Modeling NFIRAOS Rejection Transfer Functions

This appendix presents analytical expressions for the transfer functions of NFIRAOS LGS wavefront sensing problem. This is a simplified model compared to the real design, it is however useful and provides a qualitative description of the problem. It is used to assess the gain ranges of the different filters and integrators. The gain and phase margins read from Bode plots set the acceptable gain values. The results obtained with the analytical model have been cross–checked with the end–to–end Simulink® simulation and with the bench results.

The whole control system as given in Fig. 3 has been described in chapter 3 It has been shown that the control system processes tip–tilt, focus and medium orders differently. The control system can be re–written as 3 independent control systems for the tip–tilt, focus and medium orders, respectively. In the following, these systems are described as continuous systems using transfer functions expressed in the Laplace domain. Tab. B.1 gives the expressions of the transfer functions of all the components of the control system.

Transfer Function	Component	Expression
$W_{TTF}(s)$	OI TTF WFS	$\frac{1-\exp(-T_{TTF}s)}{T_{TTF}s}$
$W_{LGS}(s)$	LGS WFS	$\frac{1-\exp(-T_s s)}{T_s s}$
$W_{MOR}(s)$	MOR WFS	$\frac{1-\exp(-T_{MOR}s)}{T_{MOR}s}$
$D_{DM}(s)$	DM	$\frac{1-\exp(-T_s s)}{T_s s}$
$D_{FSM}(s)$	FSM	$\frac{1-\exp(-T_s s)}{T_s s}$
$D_{ZO}(s)$	ZO	$\frac{1-\exp(-T_{ZO}s)}{T_{ZO}s}$
$C_{FSM}(s)$	FSM integrator	$\frac{g_{FSM}}{1-z^{-1}(T_s)}$
$C_{DM}(s)$	DM integrator	$\frac{g_{DM}}{1-z^{-1}(T_s)}$
$C_{ZO}(s)$	ZO integrator	$\frac{g_{ZO}}{1-z^{-1}(T_{ZO})}$
$A_i(s)$	MF i_k average	$\frac{1-\exp(-T_{i_b}s)}{T_{i_b}s}$
$L_{i_b}(s)$	MF i_b low–pass filter	$\frac{1-\alpha'}{1-\alpha' z^{-1}(T_s)}$
$L_{fo}(s)$	OI focus low–pass filter	$\frac{g_L}{1-(1-g_L)z^{-1}(T_{TTF})}$

Table B.1: Transfer functions nomenclature. $z^{-1}(T) = \exp(-sT)$, $s = 2i\pi\nu$, ν is the frequency in Hz.

$$
\begin{aligned}
G_{TTF}(s) &= W_{TTF}(s)D_{DM}(s)C_{DM}(s) \\
G_{MOR}(s) &= W_{MOR}(s)D_{DM}(s)C_{DM}(s) \\
G_{LGS/DM}(s) &= W_{LGS}(s)\left[1 - A_i(s)L_{i_b}(s)\right]D_{DM}(s)C_{DM}(s) \\
G_{LGS/FSM}(s) &= W_{LGS}(s)D_{FMS}(s)C_{FSM}(s) \\
G_{LGS/ZO}(s) &= W_{LGS}(s)A_i(s)C_{zo}(s)D_{ZO}(s)
\end{aligned}
$$

Table B.2: Open–loop transfer functions

The tip–tilt case The tip–tilt block diagram is given in Fig. B.1. u' is the tip–tilt from the OI TTF NGS. There is no atmospheric tip–tilt coming from the LGS however, as the DM is seen by the LGS WFS, the NGS tip–tilt is measured by the LGS WFS and sent to the FSM which adds the tip–tilt to the dithering motion. This tip–tilt is cancelled with the DM NGS driven tip–tilt when the LGS light travels back to the telescope.

There are two inputs to the T/T control system: the TTF NGS tip–tilt and the dither signal. One can write the RTFs for both inputs setting each one successively to zero.

The dither signal RTF is given by:

$$\frac{y}{\text{Dither}}\Big|_{u=0} = \frac{D_{FSM}(s)}{1 + G_{LGS/FSM}(s)B(s)} \tag{B.1}$$

The NGS TTF tip–tilt RTF is written:

$$\frac{y}{u'}\Big|_{\text{Dither}=0} = \frac{G_{TTF}(s)}{\left[1 + G_{TTF}(s)\right]\left[1 + G_{LGS/FSM}(s)B(s)\right]} \tag{B.2}$$

with

$$B(s) = A_i(s)g_{LF} + \left[1 - A_i(s)L_{i_b}(s)\right]$$

.

$G_{TTF}(s)$ and $G_{LGS/FSM}(s)$ are the open–loop transfer functions of the OI TTF tip–tilt and of the LGS tip–tilt, respectively. There are given in Tab. B.2.

The focus case The focus block diagram is given in Fig. B.2. It has three inputs the TTF NGS atmospheric focus u', the LGS atmospheric focus u and the LGS focus

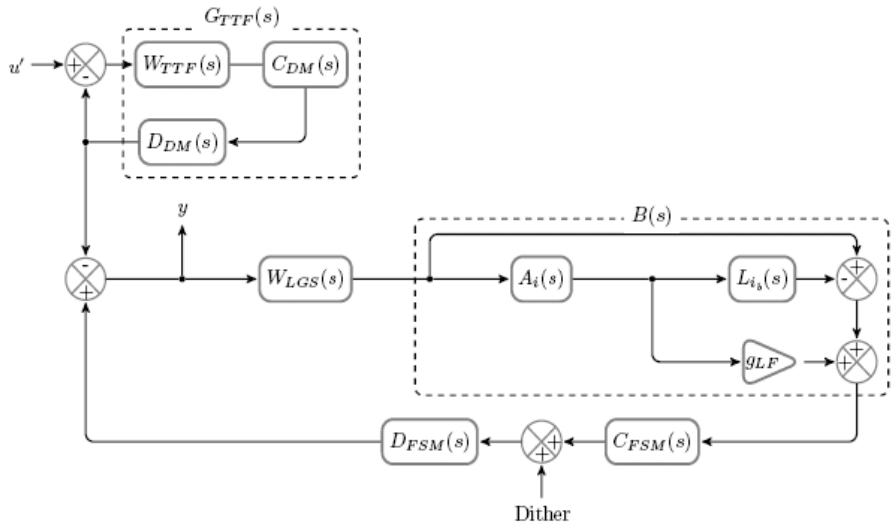

Figure B.1: T/T control block diagram.

aberration l.Assuming $u' = u$, the focus RTF is

$$\left.\frac{y}{u}\right|_{u=u',l=0} = \frac{1}{1 + G_{TTF}(s)L_{fo}(s) + \dfrac{G_{LGS/DM}(s)\left[1 - L_{fo}(s)\right]}{1 + G_{LGS/ZO}(s)}} \tag{B.3}$$

The LGS focus aberrations RTF is given by

$$\left.\frac{y}{l}\right|_{u=u'=0} = \frac{-G_{LGS/DM}(s)\left[1 - L_{fo}(s)\right]}{\left[1 + G_{LGS/ZO}(s)\right]\left[1 + G_{TTF}(s)L_{fo}(s)\right] + G_{LGS/DM}(s)\left[1 - L_{fo}(s)\right]} \tag{B.4}$$

$G_{LGS/ZO}$ and $G_{LGS/DM}$ are the open–loop transfer functions of the ZO focus and DM focus (Tab. B.2), respectively.

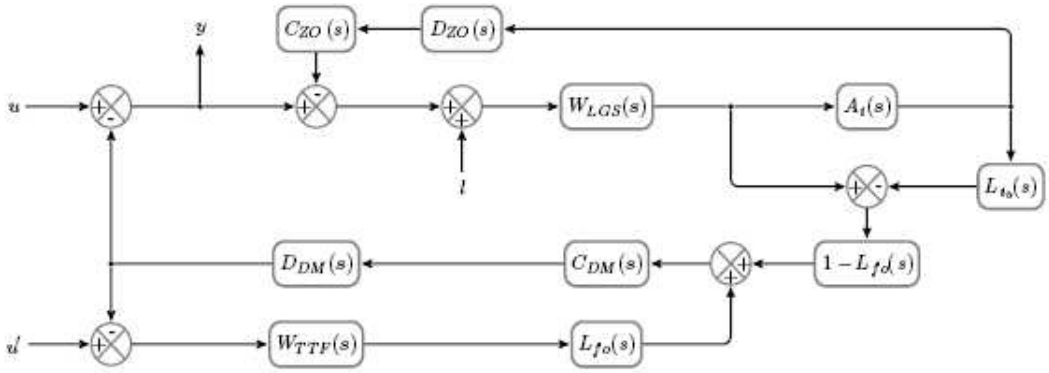

Figure B.2: Focus control block diagram.

The medium order case The medium orders control system is given in Fig. B.3. The three inputs u', u and l are the atmospheric medium orders from the MOR NGS WFS and from the LGS WFS and the Na profile induced medium orders respectively.

Here too assuming $u' = u$, the medium orders RTFs are written

$$\frac{y}{u}\Big|_{u=u',l=0} = \frac{1}{1 + G_{LGS/DM}(s) + g_{MO}G_{MOR}(s)} \tag{B.5}$$

for the atmospheric turbulence aberrations and

$$\frac{y}{l}\Big|_{u=u'=0} = \frac{-G_{LGS/DM}(s)}{1 + G_{LGS/DM}(s) + g_{MO}G_{MOR}(s)} \tag{B.6}$$

for the LGS aberrations. $G_{MOR}(s)$ (Tab. B.2) is the open–loop transfer function of the MOR WFS.

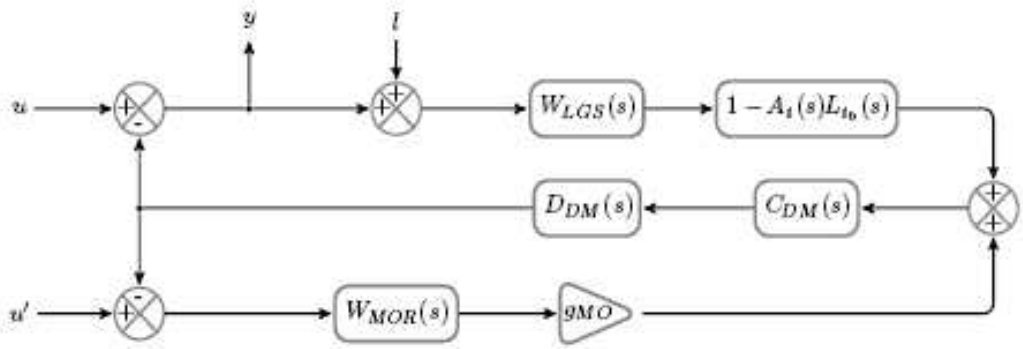

Figure B.3: Medium order control block diagram.